Mapping the Macrostructure and Microstructure of the in vivo Human Hippocampus using Diffusion MRI

Bradley G. Karat[1,2], Jordan DeKraker[1,3], Uzair Hussain[4], Stefan Köhler[5], Ali R. Khan[1,6]

[1]Robarts Research Institute, Schulich School of Medicine and Dentistry, University of Western Ontario, Canada, [2]Neuroscience Graduate Program, University of Western Ontario, Canada, [3]Montreal Neurological Institute, McGill University, Montreal, Quebec, Canada, [4]University Health Network, Toronto, Ontario, Canada, [5]Department of Psychology, University of Western Ontario, Canada, [6]Western Institute for Neuroscience, University of Western Ontario, Canada,

Data and code availability

Abstract

The hippocampus is classically divided into mesoscopic subfields which contain varying microstructure that contribute to their unique functional roles. It has been challenging to characterize this microstructure with current MR based neuroimaging techniques. In this work, we used diffusion MRI and a novel surface-based approach in the hippocampus which revealed distinct microstructural distributions of neurite density and dispersion, T1w/T2w ratio as a proxy for myelin content, fractional anisotropy, and mean diffusivity. We used the Neurite Orientation Dispersion and Density Imaging (NODDI) model optimized for gray matter diffusivity to characterize neurite density and dispersion. We found that neurite dispersion was highest in the Cornu Ammonis (CA) 1 and subiculum subfields which likely captures the large heterogeneity of tangential and radial fibers, such as the Schaffer collaterals, perforant path, and pyramidal neurons. Neurite density and T1w/T2w were highest in the subiculum and CA3 and lowest in CA1, which may reflect known myeloarchitecture differences between these subfields. Using a simple logistic regression model, we showed that neurite density, dispersion, and T1w/T2w measures provided good separability across the subfields, suggesting that they may be sensitive to the known variability in subfield cyto- and myeloarchitecture. We report macrostructural measures of gyrification, thickness, and curvature that were in line with ex vivo descriptions of hippocampal anatomy. We employed a multivariate orthogonal projective non-negative matrix factorization (OPNNMF) approach to capture co-varying regions of macro- and microstructure across the hippocampus. The clusters were highly variable along the medial-lateral (proximal-distal) direction, likely reflecting known differences in morphology, cytoarchitectonic profiles, and connectivity. Finally, we show that by examining the main direction of diffusion relative to canonical hippocampal axes, we could identify regions with stereotyped microstructural orientations that may map onto specific fiber pathways, such as the Schaffer collaterals, perforant path, fimbria, and alveus. These results highlight the value of combining in vivo diffusion MRI with computational approaches for capturing hippocampal microstructure, which may provide useful features for understanding cognition and for diagnosis of disease states.

Keywords: Hippocampus; Subfields; Microstructure; Neurite Density; Neurite Dispersion; Diffusion MRI

1. Introduction

The hippocampus is classically divided into structurally distinct mesoscopic subfields according to differences in cyto-, myelo-, and chemoarchitecture (Duvernoy et al., 2013; Ding & Van Hoesen, 2015). The neuronal circuitry that compose the microstructure of the hippocampus exist within and across these subfields. For example, the pyramidal neurons that exist within the Cornu Ammonis (CA) and subiculum subfields have apical and basal dendrites which project across the laminae, while their axons project to the alveus, a white matter bundle adjoining the hippocampus. The trisynaptic pathway is the major circuitry component which connects the subfields of the hippocampus. The entorhinal cortex connects to the dentate gyrus (DG) and other subfields through the myelinated perforant path. The DG then projects to the pyramidal neurons of CA3 through the mossy fibers, which then project to CA1 through the largely unmyelinated Schaffer collaterals. Finally, CA1 projects to the subiculum and back to the entorhinal cortex as a large hippocampal efferent. Hippocampal microstructure is key in producing unique cognitive functions such as memory formation and storage and spatial navigation among others (Voss et al., 2017; Goodroe et al., 2018; Horner et al., 2015). Furthermore, the hippocampus is typically one of the earliest aberrant structures in many disease states, where specific microstructural properties are differentially afflicted or spared (Moodley & Chan, 2014; Dhikav & Anand, 2012; Small et al., 2011). While much work has addressed volumetric characterization of the hippocampus and its subfields, understanding hippocampal microstructure can provide key insights into its complex cognitive functions as well as its early deterioration in disease.

Diffusion magnetic resonance imaging (dMRI) is a particular technique which holds promise in probing the hippocampal circuitry by sensitizing the measured MRI signal to the movement of water molecules, which diffuse more readily parallel to microstructure. Several models have been proposed that attribute measures of the dMRI signal to compartments which

102   have varying diffusivity environments (Assaf et al., 2008; Assaf & Basser, 2005; Zhang et al.,

103   2012). One of the earliest and most widely used models proposed by Basser et al. (1994) is

104   diffusion tensor imaging (DTI). DTI estimates quantitative parameters such as fractional

105   anisotropy (FA - a measure of the anisotropy of diffusion), mean diffusivity (MD – magnitude of

106   diffusion), and the ellipsoidal orientation of the diffusion process. However, DTI has some

107   notable limitations. At increasing b-values (approximately greater than 1000-1500 s/mm^2) there

108   is contribution from multiple compartments with varying diffusivities (such as restricted intra-

109   cellular water), which goes beyond the monoexponential signal modelled by DTI (Assaf &

110   Cohen. 2000). As well, regions of crossing fibers result in planar DTI ellipsoids with understated

111   FA values (Campbell et al., 2005). Furthermore, DTI measures are sensitive to multiple

112   microstructural properties at the same time, decreasing their specificity (Pierpaoli et al., 1996).

113   Other models aim to utilize increasingly complex diffusion acquisitions to relate the diffusion

114   signal attenuation to varying sets of biophysically motivated compartments.

115   One popular compartment model is Neurite Orientation Dispersion and

116   Density Imaging (NODDI), which aims to provide a biophysical interpretation of the diffusion

117   signal (Zhang et al., 2012). NODDI assumes that three microstructural environments consisting

118   of an intra-cellular, extra-cellular, and cerebrospinal fluid (CSF) compartment contribute to the

119   diffusion signal. The intra-cellular compartment is modeled as a set of infinitely anisotropic

120   sticks (diffusion can only be parallel to the main orientation of the stick), while the extra-cellular

121   compartment is modeled as a zeppelin (or cylindrically symmetric tensor) with hindered

122   diffusion perpendicular to its main axis. The CSF compartment is modeled as a sphere with

123   gaussian isotropic diffusion. Diffusion is assumed to be contained separately within each

124   compartment, where the resulting signal is the sum from all compartments. NODDI aims to

125   overcome the limitations of DTI by providing microstructural scalars such as the neurite density

126   index (NDI) and orientation dispersion index (ODI) which are sensitive to fiber crossings and are

127   biophysically grounded (Zhang et al., 2012). NDI is meant to represent the volume fraction of

128   the intra-cellular compartment, which is believed to correspond to the density of dendrites,

129   axons, and other "stick" like processes in a voxel. ODI is meant to capture the essence of the

130   orientation distribution of the diffusion signal, where more complex or disperse microstructural

131   configurations correspond to a higher ODI value.

132   Contemporary work has attempted to examine hippocampal microstructure with both DTI

133   and NODDI. Some such studies have found age-related changes of hippocampal microstructure

134   by averaging NODDI measures within subfields (Radhakrishnan et al., 2020) while others have

135   shown regionally specific changes using DTI (Yassa et al., 2010). Recent work has also begun to

136   use measures derived from structural MRI to interrogate microstructural characteristics, such as

137   the ratio of T1-weighted over T2-weighted signal as a correlate of myelin (Glasser & Van Essen,

138   2011; Glasser et al., 2014). These measures may be useful to capture the myelinated intra-

139   hippocampal circuitry like the perforant path. A recent study investigated the variation of DTI

140   and intra-cortical myelin through the ratio of T1w/T2w images across the hippocampus using

141   non-negative matrix factorization, however, they did not make quantitative comparisons of

142   microstructure within and across the subfields (Patel et al., 2020). As well, they note the limited

143   specificity nature of the DTI and T1w/T2w metrics investigated. A recent study examined the

144   distribution of NODDI metrics and cortical thickness across the entire cerebral cortex including

145   the hippocampus by averaging metrics across all subjects within each cortical parcel (Fukutomi

146   et al., 2018). Thus, they only examined coarse-grained averages across the entire hippocampal

147   volume. The spatial distributions of NODDI and DTI measures have not been extensively

148   investigated within the hippocampal subfields and across its longitudinal axis.

149   The orientation and trajectory of the hippocampal circuitry including the trisynaptic

150   circuit has been probed previously using tractography and polarized light imaging (PLI). Ex vivo

151   work has indeed resolved major parts of the hippocampal circuitry using dMRI tractography

152   (Beaujoin et al., 2018) and PLI (Zeineh et al., 2017) in a small number of samples. While these

153   studies serve as a close to ground-truth reference for the orientation of hippocampal circuitry, a

154   difficult step has been recapitulation of this circuitry in vivo. Some in vivo work has attempted to

155   use DTI to capture parts of the trisynaptic circuit such as the perforant path (Yassa et al., 2010)

156   or the whole hippocampal circuitry (Zeineh et al., 2012). However, it is unclear whether the

157   found trajectories are anatomically valid. Furthermore, at lower resolutions, tracts can be

158   spurious requiring complex acquisition and correction schemes, and since acquisitions can vary

159   across studies, tractography practically always requires separate optimization of its parameters

160   (Zeineh et al., 2012). Thus, understanding hippocampal microstructure in vivo may benefit from

161   a simpler characterization of the orientation of hippocampal circuitry with reference to metrics

162   derived from common models like NODDI within and across the subfields.

163   In the current study, we examined the spatial distribution of NODDI and DTI metrics,

164   T1w/T2w ratio, and macrostructural features of thickness, gyrification, and curvature across the

165   hippocampus using high-resolution in vivo human connectome project (HCP) data (Van Essen et

166   al., 2013), something that has not been extensively investigated. We aimed to examine if the

167   microstructural metrics systematically vary across the cytoarchitectonic defined subfields.

168   Furthermore, we used Orthogonal Projective Non-Negative Matrix Factorization (OPNNMF) as

169   a multivariate approach to capture regions of the hippocampus where these metrics co-vary. We

170   aimed to consider the current OPNNMF representation of disparate macro- and microstructural

171   metrics under the framework of previous research which has suggested modes of hippocampal

172   organization along its medial-lateral (across subfields) and anterior-posterior (longitudinal) axes

173   (Genon et al., 2021; Robinson et al., 2015; Zhong et al., 2019; Cheng et al., 2020; Plachti et al.,

174   2019; Plachti et al., 2020; Patel et al., 2020, DeKraker et al., 2020). While most hippocampus

175   representations use voxel-based approaches, we utilized a novel surface-based approach called

176   *HippUnfold* (DeKraker et al., 2018; DeKraker et al., 2022). Much like in the neocortex, surface-

177   based methods are better suited to account for interindividual differences in tissue curvature and

178   digitation than voxel-based approaches (DeKraker et al., 2022; DeKraker et al., 2021). Aligning

179   hippocampi on a 2D surface preserves topology and the known contiguity of subfields, allowing

180   for improved anatomical detail to be captured. Finally, hippocampal gray matter shows a laminar

181   distribution similar to that of other cortical areas with large radial and tangential neurite

182   components, although the highly curved structure of the hippocampus is reflected in the

183   complexity of its neurite orientations. Importantly, these neurite orientations tend to be highly

184   aligned along one of the axes of the hippocampus that span the anterior-posterior (AP

185   longitudinal), proximal-distal (PD - across subfields), or inner-outer (across laminae) directions

186   (Figure 1A and B) (Zeineh et al., 2017; Nieuwenhuys et al., 2008; Duvernoy et al., 2013). Thus,

187   we also aimed to determine if the known stereotyped orientations of microstructure can be

188   elucidated by analyzing the primary direction of diffusion along each of the axes in vivo, as

189   depicted in Figure 1B.
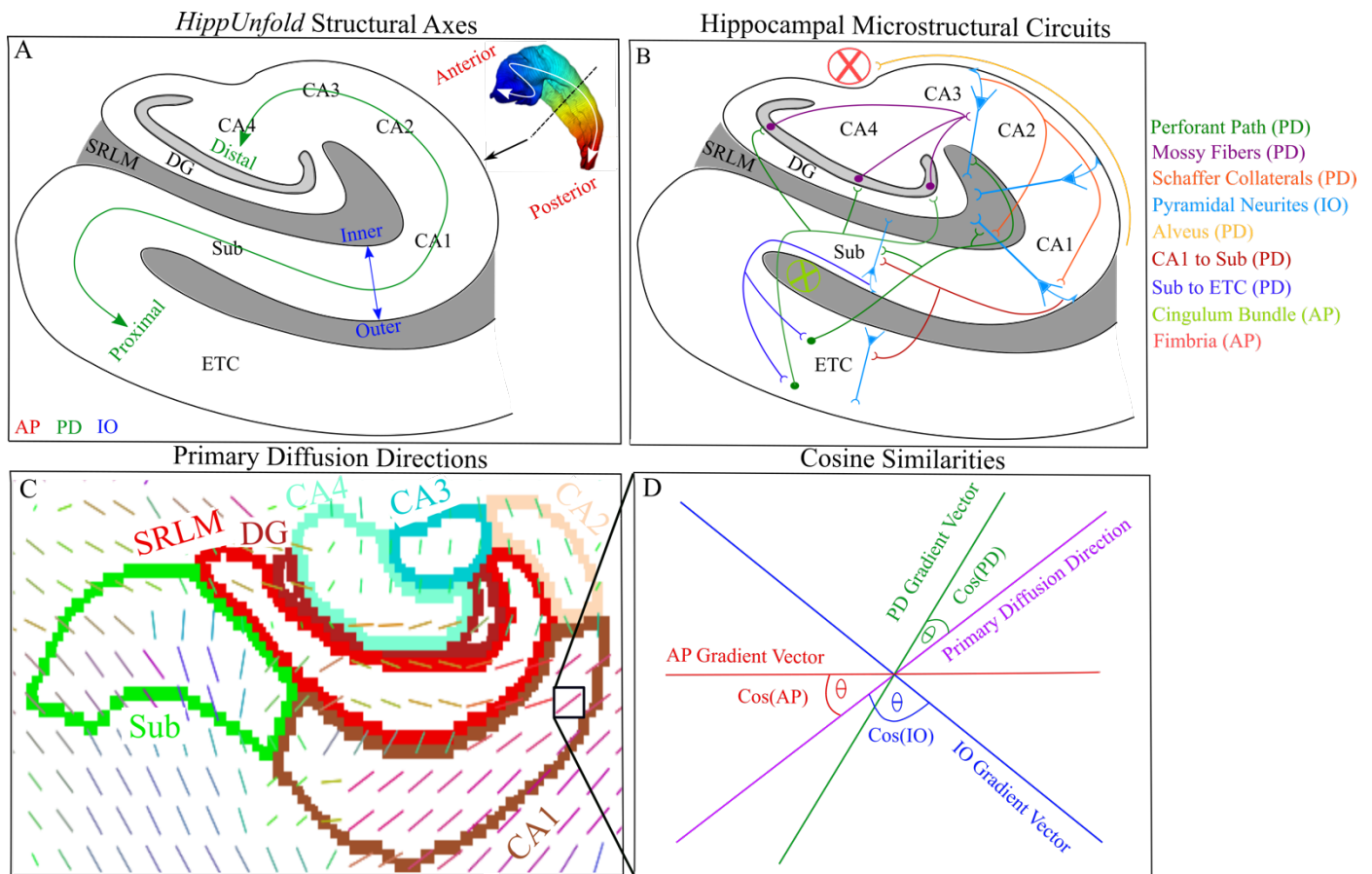
190 **Figure 1.** Depiction of hippocampal structural axes, the stereotyped organization of

191 microstructure, and diffusion vectors of the hippocampus. (A) A coronal slice depicting the

192 structural axes of the hippocampus defined as anterior-posterior (AP), proximal-distal (PD), and

193 inner-outer (IO) provided by *HippUnfold.* The inner gray area corresponds to the SRLM, while

194 the rest of the uncoloured regions correspond to the stratum pyramidale and stratum oriens

195 layers. The white arrow in the top right inset depicts the orientation of the anterior-posterior axis.

196 The colour of the hippocampal surface is the anterior-posterior Laplace coordinates. Finally, the

197 black arrow depicts the intended level of the coronal slice for the cartoon depiction. (B)

198 Simplified cartoon depiction of known microstructural circuits within the hippocampus and their

199 approximate main orientation relative to the hippocampus, defined by the colour coded legend

200 on the right (Zeineh et al., 2017; Nieuwenhuys et al., 2008; Duvernoy et al., 2013). (C) Primary

201 diffusion directions for one subject (μ of the watson distribution from NODDI) overlaid on a

202 coronal slice approximately through the hippocampal body. Coloured borders represent the

203 hippocampal subfields provided by *HippUnfold.* (D) Pictorial example representing the NODDI

204 and hippocampal axis vectors in a single voxel defined in (C). Cosine similarities are represented

205 as the angle between the NODDI vector and each hippocampal vector, providing a measure of

206 orientation coherence along each cardinal axis (see section *2.5).* Sub - Subiculum, CA - Cornu

207 Ammonis, DG - Dentate Gyrus, SRLM - Stratum Radiatum Lacunosum Meculare, ETC -

208 Entorhinal Cortex.

209 **2. Methods**

210 *2.1 Overview*

211 A subset of 100 unrelated subjects from the publicly available Human Connectome Project

212 (HCP) 1200 dataset were used for this study (Van Essen et al., 2013). All 100 subjects were run

213 through *HippUnfold* (DeKraker et al., 2022), a new automated tool for surface-based subfield

214 segmentation and hippocampal unfolding (see section *2.3*; DeKraker et al., 2018). The Laplacian

215   coordinates generated from *HippUnfold* within each subject were used to calculate gradient

216   vector fields along each axis of the hippocampus (see section *2.5 & Figure 1A). NODDI and DTI

217   metrics were calculated in each subject's native space using whole-brain diffusion images (see

218   *2.2* and *2.4*). Cosine similarities between the NODDI orientational vector (defined as μ of the

219   Watson distribution; see section *2.4*) and the vectors along each of the 3 axes (AP, PD, and IO)

220   were calculated at each voxel. Furthermore, the T1w/T2w ratio was calculated as a proxy for

221   myelin content. Macrostructural measures of curvature, gyrification, and thickness were

222   calculated along the midthickness surface (middle of the hippocampal gray matter) of the

223   hippocampus across all subjects. NODDI measures of ODI and NDI, DTI measures of FA and

224   MD, and the cosine similarities were all sampled along the midthickness surface within each

225   subject and averaged in unfolded space (DeKraker et al., 2018; DeKraker et al., 2022). Plots of

226   NODDI and DTI metrics, cosine similarities, and macrostructure metrics across the midthickness

227   surface were visualized as folded and unfolded surfaces. Logistic regression was performed at

228   the level of subfield averages using the NODDI and T1w/T2w metrics to elucidate their

229   variability across the subfields. Logistic regression was chosen due to its simplicity and

230   interpretability. Finally, Orthogonal Projective Non-Negative Matrix Factorization (OPNNMF)

231   was used to capture co-varying regions of the hippocampus and to examine the dimensions of

232   macro- and microstructure hippocampal organization.

233   *2.2 Data acquisition and preprocessing*

234   We used the publicly available HCP young adult dataset (ages 22-35), which consisted of

235   structural and diffusion MRI data for 1200 subjects (Van Essen et al., 2013). To avoid any biases

236   caused by family structures, we chose the 100 unrelated subjects subset for analysis (mean age:

237   27.52 years +/- 3.47 years; F/M: 54/46). Data included T1-weighted (T1w) and T2-weighted

238   (T2w) structural images at 0.7 mm^3 isotropic resolution and diffusion-weighted data at 1.25 mm^3

239   isotropic resolution. Structural images were obtained using a 3D MPRAGE sequence (TR-

240   2400ms, TE–2.14ms, TI-1000ms, FOV-224x224 mm). Diffusion images were obtained using a

241   spin-echo echo-planar imgaging sequence (b=0 (18 acquisitions), 1000, 2000, 3000s/mm^2, 90

242   diffusion-encoding directions, TR-5520ms, TE-89.5ms, FOV-210x180mm). Data used in the

243   preparation of this work were obtained from the Human Connectome Project (HCP) database

244   (Van Essen et al., 2013). In this work we utilized the preprocessed structural and diffusion

245   images for the HCP dataset. Preprocessing of structural images included: gradient distortion

246   correction, coregistration and averaging of repeated T1w and T2w runs using 6-DOF rigid

247   transformation, initial brain extractions for T1w and T2w, field map distortion correction and

248   registration of T2w with T1w images, bias field correction, and atlas registration. Preprocessing

249   of diffusion images included: intensity normalization across runs, EPI distortion correction, eddy

250   current and motion correction, gradient nonlinearity correction, and registration of the mean b0

251   image to T1w native space. The full pre-processing pipeline for structural and diffusion images

252   were published elsewhere (Andersson et al., 2015; Glasser et al., 2013; Jenkinson et al., 2002;

253   Sotiropoulos et al., 2013) and can be found at the HCP website

254   (https://www.humanconnectome.org/study/hcp-young-adult). To derive a correlate of myelin, we

255   divided the T1w image intensity by the T2w image intensity and corrected for the bias field

256   (Glasser & Van Essen, 2011; Glasser et al., 2014), which is referred to as T1w/T2w for the rest

257   of the paper.

258   *2.3 HippUnfold - Hippocampal unfolding and surface-based segmentation*

259   The newly developed *HippUnfold* tool was used in the current study for surface-based

260   segmentation and unfolding of the hippocampus (DeKraker et al., 2022). *HippUnfold* is

261   predicated on the idea that the hippocampal subfields are topologically constrained as they

262   differentiate from a flat cortical mantle (Duvernoy et al., 2013). Using a 'U-net' deep

263   convolutional neural network (Isensee et al., 2021), *HippUnfold* provides a detailed subject-

264   specific tissue segmentation of the hippocampal gray matter and its topological boundaries (for

265   example, the Hippocampal Amygdala Transition Area and the Indusium Griseum as the most

266   anterior and posterior topological boundaries, respectively) required for unfolding (DeKraker et

267   al., 2022). Segmentation is done for each individual hippocampi preserving its topologically

268   consistent structure, which is critical for inter-individual alignment across variably shaped

269   hippocampi. See Dekraker et al. (2022) for more detailed information on *HippUnfold.*

270   The outputs of *HippUnfold* utilized in this study included the provided subfield

271   segmentation, Laplacian coordinates for gradient field calculation (see section 2.5),

272   macrostructure measures of curvature, gyrification, and thickness, and the midthickness surface

273   representation for sampling volumetric space metrics onto the surface (see section 2.4). Due to

274   the small size of the Dentate Gyrus (DG) and CA4, we combined them into a single DG/CA4

275   subfield label. As well, portions of the DG were excluded in our surface representation. All

276   subfield segmentations for both hemispheres were reviewed for gross errors by BK. The

277   midthickness surface used in this study was composed of 2004 vertices with a spacing of roughly

278   1mm. Averaging of each metric across subjects was performed at each vertex in unfolded space.

279   *2.4 Characterization of microstructure with NODDI & DTI*

280   NODDI models the diffusion signal as a combination from 3 microstructural environments:

281   intra-cellular, extra-cellular, and cerebrospinal fluid (CSF) (Zhang et al., 2012). The intra-

282   cellular compartment is considered the space that is bounded by neurites, which is modelled as a

283   set of sticks. The stick geometry captures the restricted diffusion of water perpendicular to

284   neurites, and the relatively unhindered diffusion along them. Furthermore, sticks can capture the

285   wide range of neurite orientations, from highly coherent to highly dispersed tissue. The extra-

286   cellular compartment is the space around the neurites, which consists of glial cells and in gray

287   matter, the somas. In extra-cellular space, the signal is modeled as Gaussian anisotropic diffusion

288   to represent the hindered but not restricted movement of water. Finally, the CSF compartment is

289   modelled as Gaussian isotropic diffusion, representing the free movement of water. NODDI does

290   not draw any *a priori* assumptions about whether a voxel is gray matter, white matter or CSF,

291   and thus it treats each voxel as a possible combination of different compartments (Zhang et al.,

292   2012). Thus, the normalized dMRI signal can be written as:

293 $$E_{NODDI} = f_{iso}E_{iso}(d_{iso}) + W(\mu, \kappa)[f_{ec}E_{ec}(d_{perp}, d_{par}) + f_{ic}E_{ic}(d_{par})] \quad (1)$$

294   Where $f_{iso}E_{iso}$, $f_{ec}E_{ec}$ and $f_{ic}E_{iC}$ are the volume and signal fractions of the CSF, extra-cellular,

295   and intra-cellular (NDI) compartments, respectively. The extra-cellular and intra-cellular

296   compartments are linked orientationally by the Watson distribution $W(\mu, \kappa)$, where κ is the

297   concentration parameter (ODI $= \frac{2}{\pi}\arctan(\frac{1}{\kappa})$) and μ is the mean orientation of the Watson

298   distribution (herein referred to as the NODDI microstructural vector or primary diffusion

299   direction). The hindered perpendicular diffusion of the extra-cellular compartment d_{perp} is set via

300   a tortuosity model. The original NODDI model which was developed mainly for white matter sets

301   the parallel diffusivity value d_{par} equal to $1.7 \times 10^{-3} \frac{mm^2}{s}$ and the isotropic or CSF compartment

302   diffusion to $3.0 \times 10^{-3} \frac{mm^2}{s}$. Previous studies in the gray matter have sought to optimize d_{par}, and

303   have consistently found that the lowest mean squared error is achieved with d_{par} equal to

304    $1.1 \times 10^{-3} \frac{mm^2}{s}$ (Guerrero et al., 2019; Fukutomi et al., 2018). Thus, in the current study we

305   used the gray matter optimized d_{par} value of $1.1 \times 10^{-3} \frac{mm^2}{s}$ for fitting the NODDI model. The

306   Microstructure Diffusion Toolbox (MDT; Harms et al., 2017) was utilized to fit the NODDI model

307   using whole-brain diffusion images aligned to their respective T1w space with all b-values (b=0,

308   1000, 2000, 3000 s/mm^2). The validity of the assumptions of the NODDI model are discussed in

309   section 4.6.

310   We also used the MDT (Harms et al., 2017) to calculate metrics of FA and MD using DTI.

311   DTI was performed using only the $b = 1000 \frac{s}{mm^2}$ volumes to align with typical DTI experiments

312   (Behrens & Johansen-Berg, 2014). Both the NODDI and DTI metrics were mapped onto the

313   hippocampal midthickness surface using the process described below.

314   We used Connectome Workbench (https://github.com/Washington-

315   University/workbench) to sample values at each surface vertex from volume data. In this study

316   we used 2004 vertices defined along the midthickness surface of the hippocampus. Sampling

317   along the midthickness surface helps reduce partial volume effects. To sample voxel data along

318   the midthickness surface we used a ribbon-constrained mapping algorithm which also requires

319   the inner and outer surfaces also generated by *HippUnfold.* The ribbon method constructs a

320   polyhedron from the vertex's neighbor on each surface defined, and then estimates the volume of

321   the polyhedron that falls inside any nearby voxels to use as weights. We further reduced the

322   weight of any voxel based on its distance from the midthickness surface, where the scaling value

323   was calculated using a Gaussian with a standard deviation determined by the laminar thickness at

324   each vertex. This had the effect of more aggressively down-weighting voxels further from the

325   midthickness surface where the hippocampus is thinner. We then averaged each metric at each

326   vertex across all subjects to generate the average maps which were plotted in folded and

327   unfolded space.

328   *2.5 Examining the primary direction of diffusion relative to hippocampal axes*

329   Water molecules diffuse more readily parallel to microstructure, which in the hippocampus tends

330   to be aligned along the AP, PD, and IO axes (Zeineh et al., 2017; Nieuwenhuys et al., 2008;

331   Duvernoy et al., 2013). Thus, analyses were performed to examine how the primary direction of

332   diffusion was oriented relative to these axes, with the goal of elucidating the stereotyped

333   orientation of hippocampal microstructure (Figure 1). We obtained gradient vector fields along

334   the AP, PD, and IO axes by taking the first derivative of the respective Laplacian coordinates

335   provided by *HippUnfold* (Figure 1A), such that the vectors only pointed along one of the axes.

336 That is, we computed the partial derivative of the Laplacian coordinate function along the x, y,

337 and z spatial dimension:

$$338 \qquad \overrightarrow{G_{AP}} = \left[\frac{\partial\psi_{AP}}{\partial x}, \frac{\partial\psi_{AP}}{\partial y}, \frac{\partial\psi_{AP}}{\partial z}\right]$$

$$339 \qquad \overrightarrow{G_{PD}} = \left[\frac{\partial\psi_{PD}}{\partial x}, \frac{\partial\psi_{PD}}{\partial y}, \frac{\partial\psi_{PD}}{\partial z}\right] \qquad (2)$$

$$340 \qquad \overrightarrow{G_{IO}} = \left[\frac{\partial\psi_{IO}}{\partial x}, \frac{\partial\psi_{IO}}{\partial y}, \frac{\partial\psi_{IO}}{\partial z}\right]$$

341 Where the function ψ_* represents the spatial Laplacian coordinates along a particular

342 hippocampal axis (AP, PD, or IO), which were calculated by solving Laplaces equation along

343 each axis ($\nabla^2(\psi) = 0$) (DeKraker et al., 2022). The result was 3 distinct vector images within a

344 hemisphere for each subject and axis. With the aligned NODDI microstructural vectors

345 (representing the primary diffusion direction), we calculated cosine similarities between the

346 generated vectors along the AP, PD, and IO axes and the NODDI microstructural vector at each

347 voxel (Figure 1C & D). All vectors were normalized before calculating cosine similarities. The

348 cosine similarity was defined as the inner product between vectors:

$$349 \qquad \mathrm{abs}\left(\frac{\bar{a}\cdot\bar{u}}{|\bar{a}|\,|\bar{u}|}\right) \qquad (3)$$

350 Where $\bar{a}$ was a hippocampal axis vector in a single voxel (AP, PD, or IO), and $\bar{u}$ was the

351 NODDI microstructural vector (μ of the Watson distribution) at the same voxel. A higher cosine

352 similarity meant that diffusion is increasingly oriented along that hippocampal axis (cosine

353 similarities of 0 and 1 correspond to angles of 90 degrees and 0 degrees, respectively). The

354 cosine similarities were then put into context of the known spatial arrangement of hippocampal

355 microstructure and their stereotyped orientation (Figure 1A and B) under the assumption that the

356 primary direction of diffusion modelled the main microstructural orientation at each voxel. There

357 were a total of 3 cosine similarity images (one for AP, PD, and IO similarity values) within each

358   hemisphere for each subject. Each scalar cosine similarity image was sampled along the

359   midthickness surface and averaged as described above.

360   *2.6 Correlations between all metrics*

361   Spearman correlations were performed at both the subject-level and at the level of the vertex

362   averaged maps (Figure 2C-J average maps). However, it is difficult to test the significance of the

363   spatial correspondence between maps. One proposed solution that has been implemented using

364   the spherical representation of the cortical surface has been to perform spin testing, where the

365   cortical sphere is randomly permuted to derive a null distribution of association which preserves

366   the spatial autocorrelation in the data (Alexander-Bloch et al., 2018). Critically, the geometry of

367   our unfolded hippocampus cannot be well represented by a sphere. We thus developed a similar

368   method on the unfolded hippocampus. Our developed method uses periodic boundary conditions

369   on the unfolded plane, which can be thought of as performing spin testing on a torus geometry.

370   This allows us to perform rotations and translations and thus derive permuted null distributions.

371   We then used this hippocampal spin test to analyze the significance of the observed associations

372   between the averaged maps. We performed 2500 permutations between any two averaged maps,

373   and we then performed false-discovery rate correction on the derived p-values using the

374   Benjamini-Hochberg method. Technical and practical background on the developed

375   hippocampal spin test can be found in Supplementary Document 1, and the spin test code can be

376   found at Karat (2023).

377   *2.7 Orthogonal Projective NNMF (OPNNMF)*

378   Orthogonal Projective NNMF (OPNNMF) was used in this work to attempt to identify co-

379   varying regions in the hippocampus using the metrics described above (Sotiras et al., 2015; Yang

380   & Oja, 2010). OPNNMF decomposes an input matrix X of dimensions a x b into a component

381   matrix C (a x k) and a weight matrix W (k x b). The number of components (k) is defined *a*

382   *priori*. The component and weight matrices are derived such that their multiplication best

383   reconstructs the input data (X ~ C x W). OPNNMF solves the following minimization problem

384   to estimate C (Sotiras et al., 2015):

385    $$\|X - CC^TX\|^2 \text{ subject to } C \geq 0, C^TC = I, \text{ and } W = C^TX \qquad (4)$$

386   Where || || ^{2} represents the squared Frobenius norm and I denotes the identity matrix which

387   enforces orthogonality among C. C is first initialized using a non-negative double singular value

388   decomposition (Boutsidis & Gallopoulos, 2008). Then, C is updated through an iterative process

389   until it converges on an optimal solution. The iterative multiplicative update rule is as reported by

390   Yang and Oja (2010):

391    $$\grave{C}_{ij} = C_{ij} \frac{(XX^TC)_{ij}}{(CC^TXX^TC)_{ij}} \qquad (5)$$

392   Where i represents the number of vertices and j represents the number of components. The

393   component matrix C represents the latent structure in the data and allows for an examination of

394   the underlying covariance in multivariate data. As done in Patel et al. (2020) the sparse and non-

395   overlapping component matrix allows for each vertex to be assigned an output component using a

396   winner take all method which improves the interpretability of the spatial output components. The

397   weight matrix W represents the subject-metric coefficients, allowing for an examination of subject-

398   specific and metric-specific contributions to each component.

399   *2.8 Implementing OPNNMF*

400   A total of 11 metrics were included in the OPNNMF implementation (ODI, NDI, T1w/T2w, FA,

401   MD, gyrification, thickness, curvature, AP cosine similarity, PD cosine similarity, IO cosine

402   similarity) with subsets of these metrics used for more specific analyses (i.e. NODDI only, DTI

403   only, macrostructure only, and cosine similarity only). The input matrix X was built using all

404   2004 vertices of the midthickness surface in unfolded space for all 11 metrics across all 100

405   subjects per hemisphere. That is, each subject contributed 11 unfolded space maps to the input

406   matrix. Thus, the input matrix had 1100 columns (100 subjects x 11 metrics - defined as subject-

407   metrics) and 2004 rows (2004 vertices) for a single hemisphere. Normalization was required

408   since the metrics exist on different scales. First, each metric was z-scored within each

409   hemisphere. Then, each z-scored metric distribution was shifted by the minimum value from all

410   the z-scored metrics to ensure all metrics were on the same scale and there were no negative

411   values. All distributions were manually inspected to ensure the minimum value used was not an

412   outlier.

413   OPNNMF was implemented using publicly available and open MATLAB code at

414   https://github.com/asotiras/brainparts (Sotiras et al., 2015; Yang & Oja, 2010; Boutsidis &

415   Gallopoulos, 2008; Halko et al., 2011). OPNNMF was run with a max number of iterations =

416   10000, tolerance = 0.00001, and non-negative double singular value decomposition initialization.

417   *2.9 Stability & Reconstruction Error*

418   The quantification of OPNNMF decomposition stability followed that of Patel et al. (2020).

419   Stability was assessed by examining the similarity of the spatial component matrix C across

420   varying splits of data. All 100 subjects were randomly split into two groups of equal sizes.

421   OPNNMF was then performed on each split independently. A within-split similarity matrix was

422   then derived by multiplying a particular splits component matrix by the transpose of itself (i.e. a

423   cosine similarity). The result is a 2004x2004 (number of vertices x number of vertices) matrix

424   where each row contains the cosine similarity of component scores between a vertex and all

425   other vertices. Finally, a Pearson's correlation coefficient was calculated across the rows of the

426   cosine similarity matrix between splits to quantify if the decomposition maintained the

427   relationships between vertices. The above process was repeated 6 times, each with a new random

428   split of the data. The mean and standard deviation of the correlation coefficient was taken across

429   all vertices and splits for a given component solution. A correlation of 1 represented perfect

430   stability (i.e. each split of the data had perfect correspondence between vertex relationships),

431   whereas -1 represented instability. The above process was then repeated for different component

432   decompositions, from k=2 to k=12. Reconstruction error was calculated through 3-steps. First,

433   the component matrix C and the weight matrix W were estimated and then multiplied together to

434   return the reconstructed input matrix. The original and reconstructed input matrix were then

435   subtracted to obtain a reconstruction error matrix. The Frobenius norm of the reconstruction

436   error matrix was then taken to get the reconstruction error. The gradient in the reconstruction

437   error was taken across solutions with varying component numbers to assess the magnitude of the

438   improvement in reconstruction error when adding more components.

439   *2.10 Interpreting OPNNMF*

440   The output component matrix C contains a component value for each vertex while the weight

441   matrix W describes how each subject-metric is projected onto each component. A large value in

442   the component matrix can be interpreted as a particular vertex being identified as a part of the

443   variance pattern. The weight matrix can be used to elucidate which metrics contributed to each

444   component as well as inter-subject variance within metrics. In the current study these 2 matrices

445   were used to explore spatial patterns and the contributions of particular metrics to each

446   component. A winner-take-all method was used where a vertex was assigned the integer of the

447   component with the highest component weighting value from the matrix C. The matrix W was z-

448   scored within each component row and then plotted to examine metric-specific trends.

449   **3. Results**

450   The results begin with qualitative descriptions of average macro- and microstructural measures

451   and their correlations on the midthickness hippocampal surface (middle of the hippocampal gray

452   matter). We also show the significance of these correlations using the developed hippocampal

453   spin test. We then present results from a logistic regression model used to examine the

454   separability of the subfields using microstructural features. We then show the cosine similarities

455   between NODDI microstructural vectors and the hippocampal axis vectors. Finally, we present

456   the OPNNMF results including a stability analysis and a 6-component solution.

3.1 Distributions of Hippocampal Metrics

Figure 2 presents Spearman's rho correlations, mean macro- and microstructural metrics, along with subfield segmentations shown on an averaged hippocampal midthickness surface in folded and unfolded space. The standard deviation of these metrics is shown in supplementary Figure 1. The orientation dispersion (ODI - Figure 2C) is highest in the anterior and body of CA1 and the distal parts of the subiculum, while dispersion is lowest in the body and posterior of DG/CA4, CA3 and CA2 and at the most proximal edge of the subiculum. Neurite density (NDI - Figure 2D) is highest in the body and tail of the subiculum, while there is lower neurite density in CA1 and the DG/CA4. The T1w/T2w ratio has a strikingly similar distribution to that of NDI, as found in previous cortical studies (Figure 2E; Fukutomi et al., 2018). T1w/T2w, ODI, and NDI maps appear to vary across the subfields.

Macrostructure features of thickness, gyrification, and curvature are shown in Figure 2H-J. Gyrification is largest in anterior CA1 and the DG/CA4. The thickest regions are the anterior and posterior of the subiculum and CA1, as well as throughout the DG/CA4, while CA3 and CA2 are thin. Curvature tends to be highest in the anterior part of the subiculum, along the spine of the hippocampus (red arrows in Figure 2J), and in CA3. These findings are largely in line with previous work (DeKraker et al., 2020).

Spearman's rho correlations between averaged maps of these metrics can be seen in the lower triangle of Figure 2A while the false-discovery rate (FDR) corrected p-values derived from the hippocampal spin test can be seen in the upper triangle. Similar correlations between all maps at the subject level can be seen in supplementary Figure 2. The null distributions given by the spin test using the averaged maps can be seen in supplementary Figure 3.

3.2 Correlations between NODDI metrics & T1w/T2w

In Figure 2D and E, strong qualitative similarities can be seen between NDI and T1w/T2w. Both are high in the subiculum and CA3/CA2 regions, while hypointensities are noted in CA1. A

482   significant spatial overlap is seen between the positively correlated NDI and T1w/T2w maps (ρ

483   = 0.86, FDR corrected p-value < 0.05). ODI (Figure 2C) and T1w/T2w (Figure 2D) are also

484   significantly overlapping and are negatively correlated (ρ = -0.61, FDR corrected p-value <

485   0.05). A similar correlation has also been noted across the entire cortex (Fukutomi et al., 2018).

486   *3.3 Correlations between NODDI & DTI metrics*

487   Qualitatively, the map of FA (Figure 2F) resembles the NDI map (Figure 2D) and the inverse of

488   the ODI map (Figure 2C). Particularly, the distinct pattern of high dispersion equates to low FA,

489   while high neurite density equates to high FA. Furthermore, the region of low neurite density

490   (Figure 2D) in the body of CA1 and CA2 corresponds to a region of high MD (Figure 2G). ODI

491   and FA have a significant spatial overlap and are negatively correlated (ρ = -0.88, FDR corrected

492   p-value < 0.05). Furthermore, NDI and FA are significantly overlapping and are positively

493   correlated (ρ = 0.75, FDR corrected p-value < 0.05) and NDI and MD are significantly

494   overlapping and negatively correlated (ρ = -0.46, FDR corrected p-value < 0.05).

495   A disentangling of FA as determined by ODI and NDI has been reported previously in

496   cortical gray matter (Zhang et al., 2012). Two voxels with different neurite densities can have the

497   same FA if the one with the larger neurite density also has the larger dispersion (Zhang et al.,

498   2012). That is, anisotropy as measured with FA conflates neurite density and orientation

499   dispersion. We report a similar level of disentangling within the hippocampus in supplementary

500   Figure 4, where within any bin of FA there is a range of potential ODI and NDI values.

501   *3.4 Correlations between macrostructure and NODDI metrics*

502   The only significant overlap between a macrostructural and microstructural map is gyrification

503   and T1w/T2w, which are negatively correlated (ρ = -0.46, FDR corrected p-value < 0.05).

504   Regions of high gyrification in CA1 spatially correspond to regions of low T1w/T2w content.

505   While there are some other notable correlations, such as a moderate positive correlation between

506   gyrification and ODI (ρ = 0.45) and a moderate negative correlation between gyrification and

507   FA (ρ = -0.49), none were significantly overlapping. Correlations between NODDI and

508   macrostructural measures at the subfield-averaged level can be seen in supplementary Figure 5.
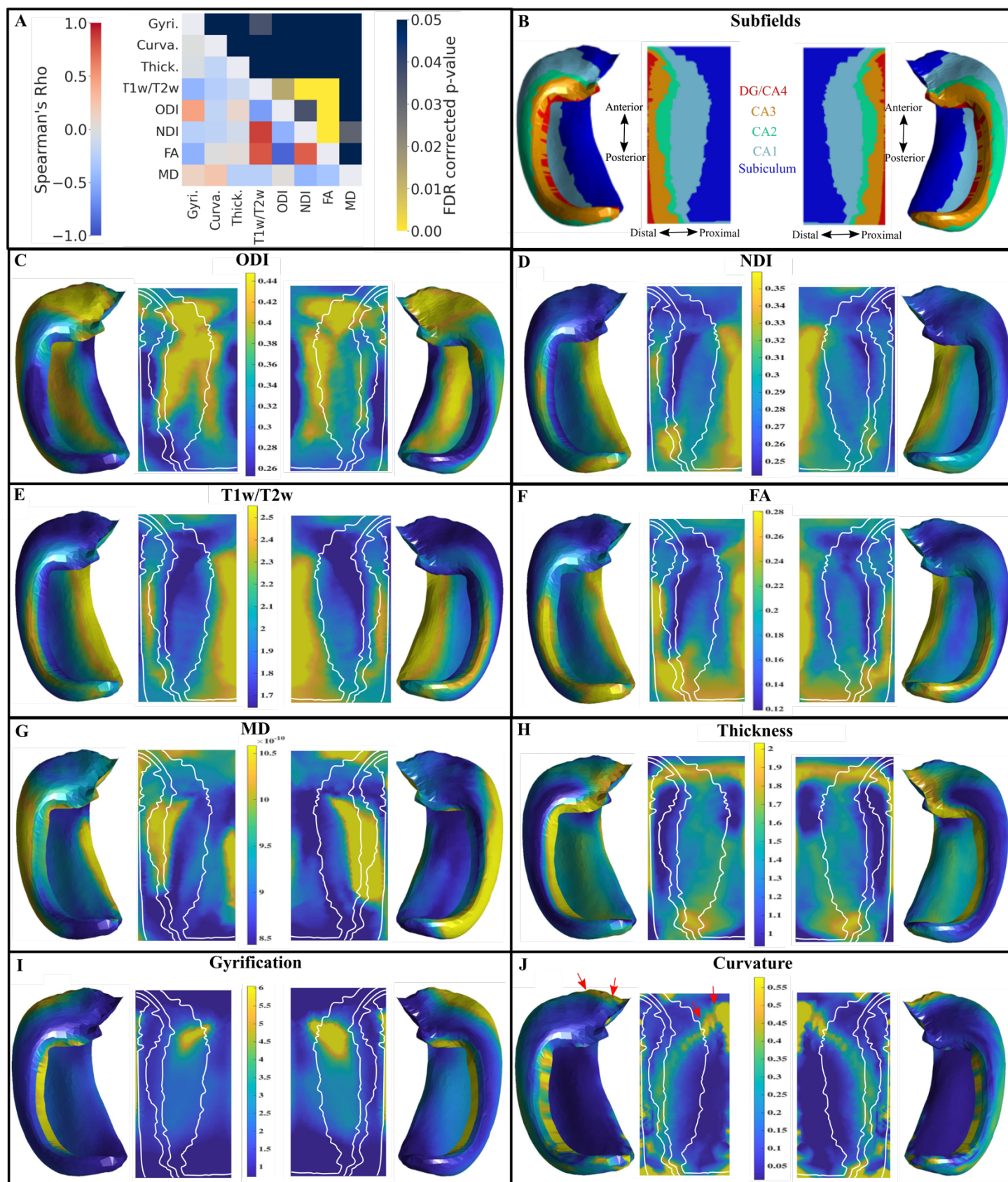
509　**Figure 2.** Correlations and plots of mean macro- and microstructure metrics on averaged

510　hippocampal midthickness surfaces in folded and unfolded space for left and right hemispheres.

511　(A) Lower triangle of the heatmap shows the Spearman's rho correlations of the average maps

512　after combining both left and right hemispheres. The upper triangle represents the false-

513　discovery rate corrected p-values derived from the hippocampus spin testing using 2500

514　permutations. Note that the colour bar is inverted such that any brighter component of the

515　heatmap corresponds to a significant p-value. (B) Left and right hippocampal subfields from a

516　manual segmentation of a histological reference (Ammunts et al., 2013; DeKraker et al., 2020).

517　Unfolded space is shown in the same orientation for left and right hemispheres. DG - Dentate

518　Gyrus, CA - Cornu Ammonis. (C,D) Orientation Dispersion Index (ODI) and Neurite Density

519　Index (NDI) from NODDI. White lines represent subfield borders shown in (B). (E) T1w/T2w

520　ratio. (F,G) Diffusion Tensor Imaging metrics of Fractional Anisotropy (FA) and Mean

521　Diffusivity (MD - m^2/s). (H-J) Macrostructure measures of thickness, gyrification, and

522　curvature. (J) Red arrows highlight the highly curved "spine" of the hippocampus.

523　*3.5 Evaluating the variability of the microstructural metrics across the subfields*

524　To examine if the microstructural metrics used here could provide differentiability to the

525　subfields, we trained a simple logistic regression classifier with L2 regularization on subfield

526　averaged microstructural measures using the scikit-learn (version 1.1.2) package in python

527　(Pedregosa et al., 2011). 70 subjects were included in the training set, while 30 subjects were

528　included in the testing set (both hemispheres were combined). ODI, NDI, and T1w/T2w

529　averages across the midthickness surface within each of the 5 subfields per hemisphere were

530　obtained within each subject in both the training and testing set. A logistic regression model was

531　then trained to predict the subfield label given the subfield averaged microstructural metrics.

532　This model was then tested on the unseen data from the testing set to quantify if the

533　microstructural metrics are differentiable across the subfields. Examining all the data points for

534   ODI, NDI, and T1w/T2w, colour coded by subfield class, it appears that the subfields present as

535   relatively separable clusters apart from CA2 which appears to have lots of microstructural

536   overlap with the other subfields (Figure 3A). The same clustering can be seen in the test set

537   (Figure 3B) left out to evaluate the performance of the logistic regression classifier (Figure 3C).

538   Using a confusion matrix and F1-scores defined as (2*precision*recall) / (precision+recall), it

539   can be seen that the simple logistic regression classifier was able to perform well in delineating

540   the subiculum (F1-score = 0.87), CA1 (F1-score = 0.85), CA3 (F1-score = 0.69), and the

541   DG/CA4 (F1-score = 0.83) using microstructural measures of ODI, NDI, and T1w/T2w (Figure

542   3D). However, CA2 was not as differentiable from the rest of the subfields using these metrics,

543   with an F1-score of 0.53. Furthermore, we found that ODI and NDI generally had higher F1-

544   scores and greater separability across the subfields then the DTI metrics of FA and MD

545   (supplementary Figure 6).
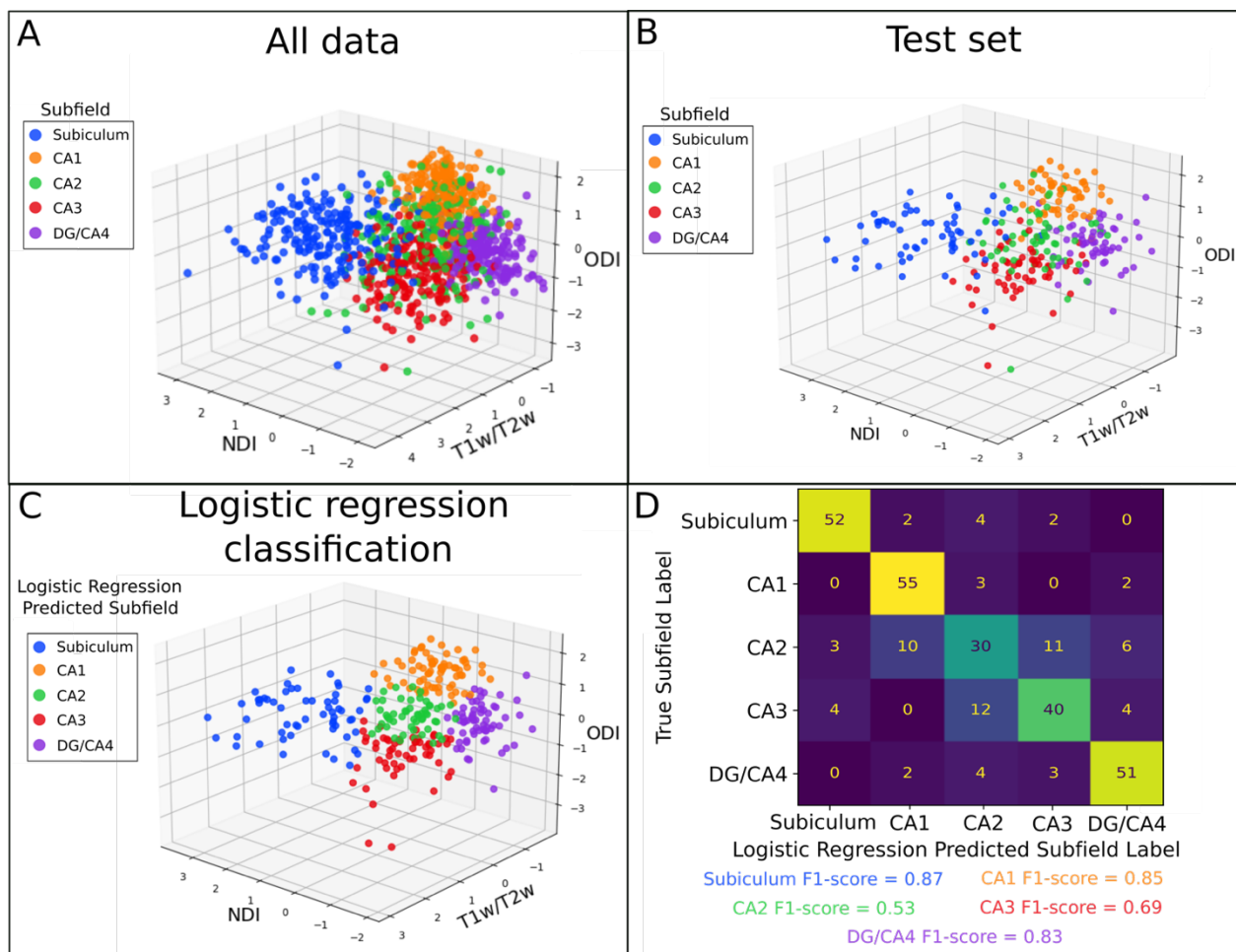
546   **Figure 3.** The performance of a logistic regression classifier to capture microstructural

547   variability across the subfields. (A) Subfield averaged ODI, NDI, and T1w/T2w from all subjects

548   and hemispheres combined coloured by subfield label. (B) Test set data from 30 subjects

549   coloured by subfield. (C) Logistic regression classified labels on the test set seen in (B). (D)

550   Confusion matrix and subfield-specific F1-scores to evaluate logistic regression performance on

551   classifying the subfields using the microstructural measures of the test set.

552   *3.6 Examination of the primary direction of diffusion relative to hippocampal axes*
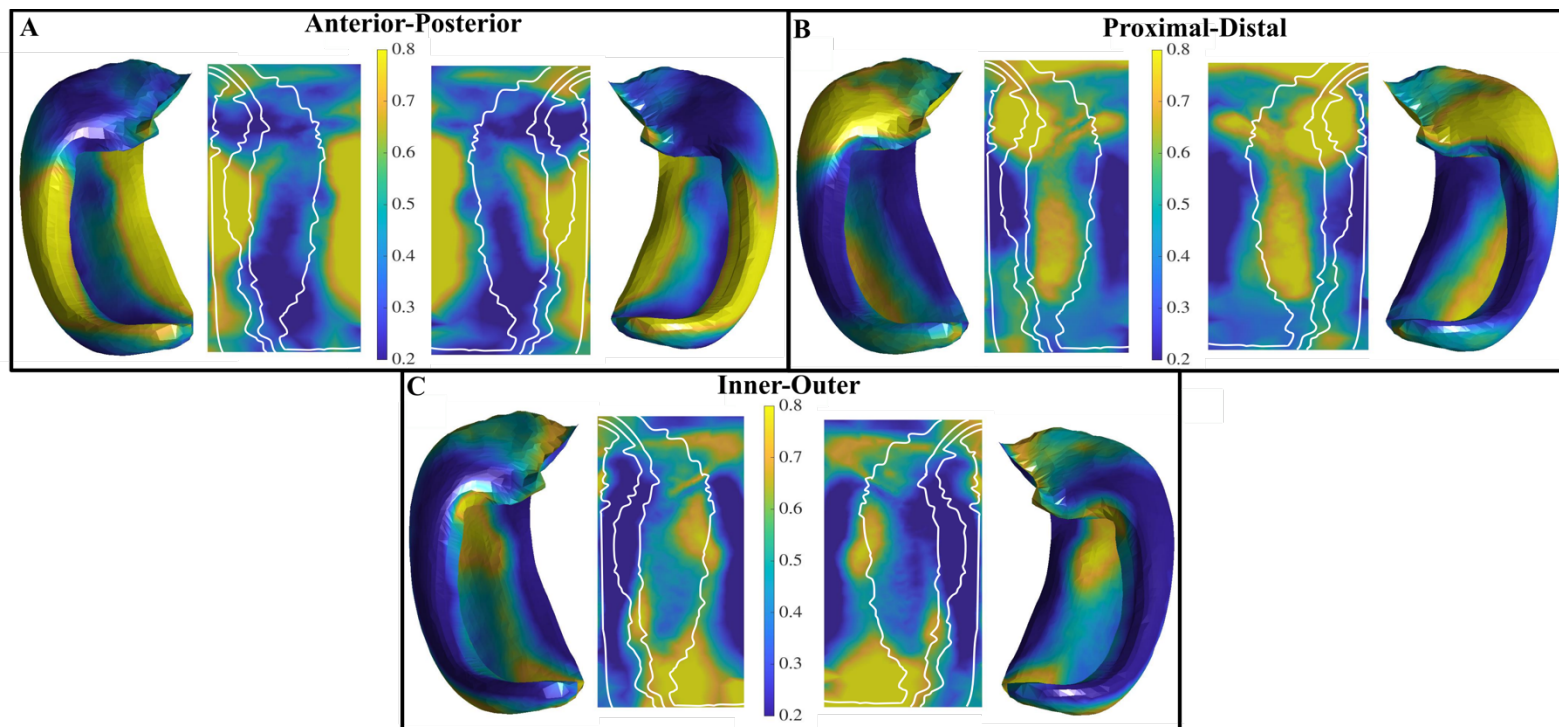
553   This section qualitatively analyzes the mean of the cosine similarities (Figure 1D; Figure 4)

554   between the hippocampal vectors along the anterior-posterior (AP), proximal-distal (PD), and

555   inner-outer (IO) (Figure 1A) axes and the NODDI microstructural vectors along the

556   midthickness surface (Figure 1C).

557   High AP alignment can be seen in the body of the DG to CA3, as well as in the

558   subiculum. Furthermore, there is relatively little AP oriented diffusion in CA1.

559   High PD oriented diffusion can be seen in the head of CA3, CA2, CA1, and in the body

560   of CA1. There was little PD oriented diffusion in the body of DG/CA4, CA3, CA2, and the

561   subiculum.

562   High IO alignment can be seen in the tail of the subiculum and CA1, as well as

563   throughout the body of CA1, while low IO oriented diffusion can be seen in the body of the

564   DG/CA4, CA3, CA2, and the subiculum.

565   The cosine similarities varied the greatest in CA1 and the subiculum across AP, PD, and

566   IO directions (supplementary Figure 7). Noticeable differences in the orientation of diffusion

567   across the subfields can be seen in supplementary Figure 8.

Figure 4. Mean of the cosine similarities between hippocampal axis vectors and NODDI microstructural vectors in the left and right hemisphere along the midthickness surface. High cosine similarities correspond to a high alignment of the NODDI microstructural vector along that particular hippocampal axis. (A) Distribution of cosine similarities along the anterior-posterior direction. (B) Distribution of cosine similarities along the proximal-distal (tangential) direction. (C) Distribution of cosine similarities along the inner-outer (laminar) direction.

3.7 Stability Analysis

The results of the stability analysis can be seen in Figure 5. Figure 5A presents the stability and the gradient in the reconstruction error using all the metrics combined that are shown in Figure 5B-E. The goal of the stability analysis was to elucidate the largest component value that was still stable and provided a relative gain in reconstruction error. In Figure 5A it can be seen that a component solution of k=6 has good stability with relatively low standard deviation. Comparatively, decomposing into a larger number of components decreases the stability of the OPNNMF solution. As well, k=6 does provide a relative gain in reconstruction error, although the largest gain in reconstruction error occurs when moving from a k=2 to a k=3 solution. The

583   stability analysis suggests that k=6 is the highest component value that is largely stable, thus we

584   use this for the decomposition results using all metrics.
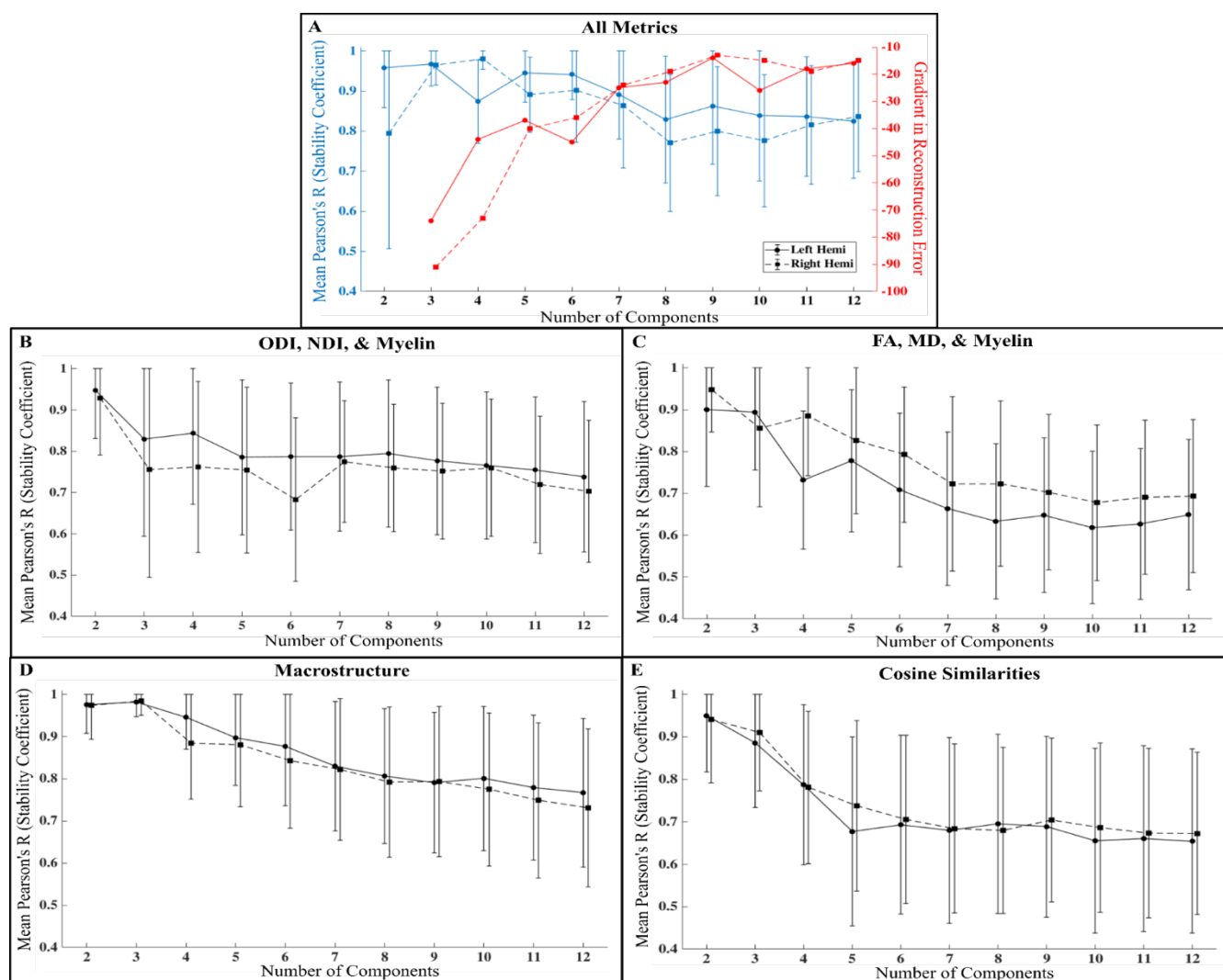
585   **Figure 5.** Stability coefficient and the gradient in reconstruction error based on the number of

586   components used for the OPNNMF solution. Filled in circles plus solid lines are the left

587   hemisphere and filled in squares plus dotted lines are the right hemisphere. Error lines show +/-

588   1 SD. (A) Stability coefficient (blue) and the gradient in reconstruction error (red) as a function

589   of the number of components using all metrics for NMF in B-E. (B) Stability coefficient for

590   NODDI metrics (ODI and NDI) plus T1w/T2w. (C) Stability coefficient for DTI metrics (FA

591   and MD) plus T1w/T2w. (D) Stability coefficient for macrostructure metrics (gyrification,

592   thickness, curvature). (E) Stability coefficient for cosine similarities (AP, PD, and IO). Points

593   between hemispheres are slightly offset along the x-axis so that error bars are visible.

594   Another goal of the stability analysis was to compare the stability of the decomposition

595   using all metrics versus using smaller groupings of metrics, such as NODDI (ODI and NDI) plus

596   T1w/T2w. Comparing Figure 5A with Figure 5B-E, it can be seen that for almost all component

597   values the all metric solution tends to be more stable than any of the smaller metric groupings.

598   This is especially true for the larger component values above k=6. These results suggest that the

599   use of multiple metrics results in more stable parcellations, as found in Patel et al. (2020).

600   The 6-component solution using all metrics is presented in Figure 6 for both the left and

601   right hippocampus. 4, 5, 6, and 7-component solutions using all the metrics can be found in

602   supplementary Figure 9. 4-component solutions for all smaller metric combinations shown in

603   Figure 5B-E can be found in supplementary Figure 10.

604   *3.8 Description of the 6-component Solution*

605   Figure 6A depicts the winner-take-all method applied at each vertex in folded and unfolded

606   space for 6-components. Figure 6B shows the z-scored subject-metric weight matrices. In the

607   following paragraph we describe the first 3 components including their location relative to the

608   subfields (proximal-distal/medial-lateral axes) as well as along the anterior-posterior

609   (longitudinal) axis. We then briefly describe components 4-6. We also describe the features

610   which contribute to each component. The left and right hippocampus do have similar covariance

611   patterns although the component ordering differs. For example, the vertices of left component 1

612   correspond to the vertices of right component 2. To simplify our descriptions, we take the

613   ordering of the left hippocampus for the rest of the paper, and we have made this adjustment

614   such that the difference in ordering does not need to be considered for Figure 6 (Patel et al.,

615   2020).

616   Component 1 is characterized by a cluster of vertices through the body and tail of the

617   most proximal edge of the subiculum and through the body and tail of CA3. This component

618   spans around the bottom two-thirds of the hippocampus across its anterior-posterior axis.

619   Component 1 is characterized by high NDI, T1w/T2w, FA, and AP cosine similarity, with lower

620   ODI, PD and IO cosine similarity. This may reflect the large anisotropic AP oriented fiber

621   bundles that are myelinated such as the cingulum bundle for the proximal edge of the subiculum

622   and the fimbria for CA3.

623   Component 2 is characterized by vertices that are present only in the body or middle one-

624   third along the anterior-posterior axis of CA1. This component is characterized by high ODI,

625   gyrification, and PD and IO cosine similarities. This likely reflects a high heterogeneity in fiber

626   orientation in CA1.

627   Component 3 is characterized by vertices that cross the subiculum and CA1 in a

628   proximal-distal fashion in the head of the hippocampus, as well as vertices that span the anterior-

629   posterior body of the hippocampus at the border between the subiculum and CA1. This

630   component is characterized by high ODI, thickness, and IO cosine similarity.

631   Component 4 corresponds to a large posterior cluster that stretches into the body of CA1

632   characterized by a moderate range of metrics with the largest being the PD cosine similarity and

633   FA. Component 5 corresponds to a cluster of vertices in the body of CA2 and CA1 and is

634   represented by a large MD, curvature, and AP cosine similarity and low NDI, T1w/T2w, FA, and

635   thickness. Interestingly, component 6 is characterized by a thin cluster of vertices roughly

636   corresponding to the anterior and body of the DG/CA4 region. This was represented by high

637   macrostructural measures of thickness, gyrification, and curvature and low weights for all other

638   metrics.

639   A general pattern is noticed when examining the whole 6-components rather than looking

640   at its parts. Generally, more parcellations exist along the proximal-distal direction than do in the

641   anterior-posterior direction.
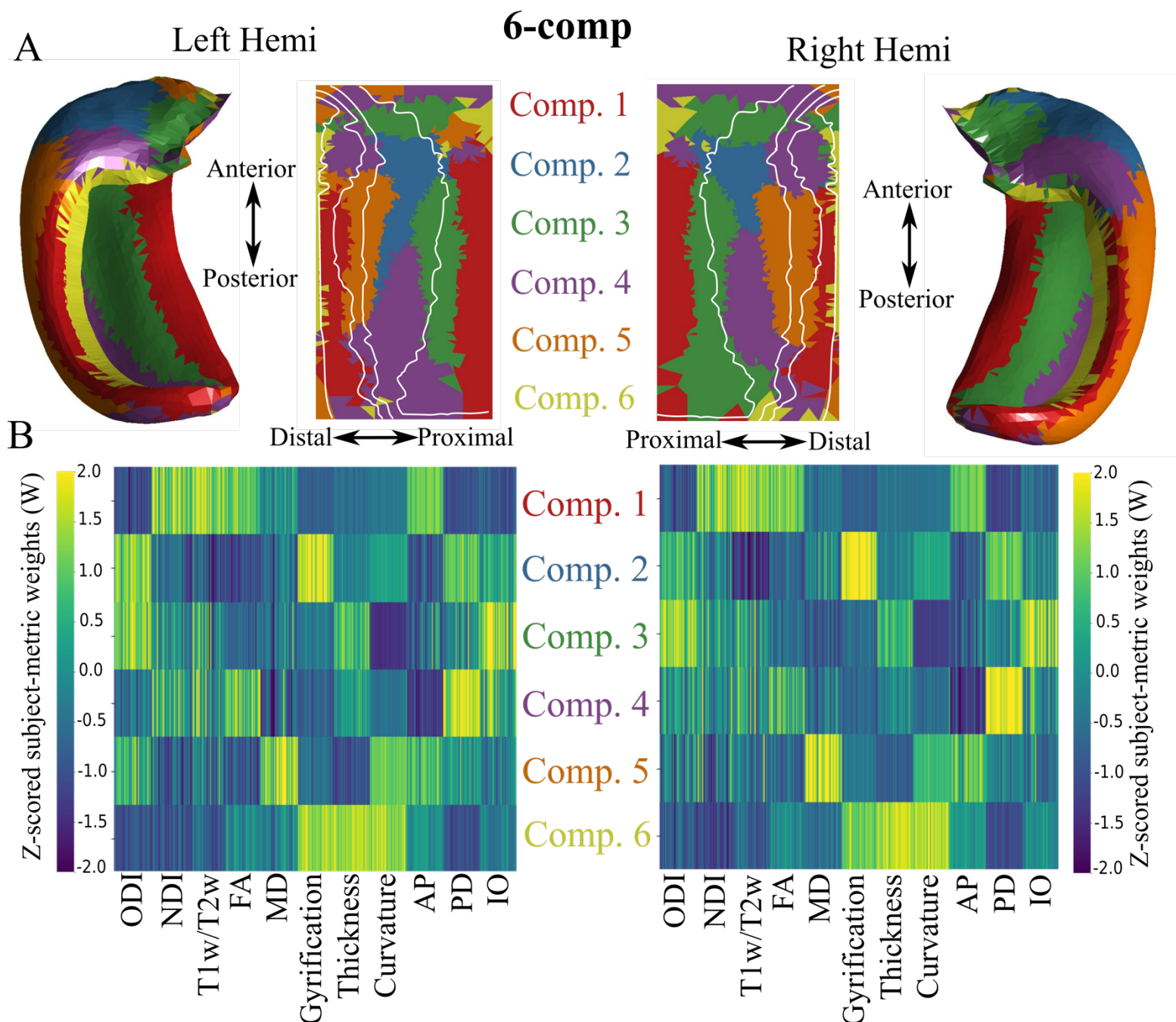
Figure 6. 6-component NMF solution on the midthickness surface for left and right hippocampi. (A) Winner-take all output at each vertex shown in folded and unfolded space. White lines denote subfield borders. (B) Z-scored subject-metric weight matrices across each of the 6 components, denoting the z-scored contribution of each metric to each component. AP, PD, and IO represent the 3 cosine similarity metrics.

647 **4. Discussion**

648 In the current study we examined the microstructure of the hippocampus using the in vivo HCP

649 dMRI and structural data, along with a novel surface-based method for subfield segmentation. We

650 found that ODI was highest in the CA1 subfield, likely capturing the large heterogeneity of

651 tangential and radial fibers. NDI and T1w/T2w were found to be strongly correlated and were

652 highest in the subiculum and lowest in CA1 and the DG/CA4, suggesting that NODDI is likely

653 sensitive to the myelin content of the hippocampus. Using these microstructural measures, we

654 found that the cytoarchitectonic defined subfields were largely separable using a simple logistic

655 regression model. OPNNMF components appeared to capture unique co-varying clusters within

656 the hippocampus, with high medial-lateral variability. Finally, we showed distinct regions of

657 similar microstructural orientations by examining the main direction of diffusion relative to the

658 three hippocampal axes, which may correspond to specific microstructural properties.

659 *4.1 Dispersion of neurites in the hippocampus may reflect heterogeneous radial and tangential*

660 *neurite components*

661 The Orientation Dispersion Index (ODI) is meant to characterize the variation in diffusion

662 orientations around a single dominant direction at every voxel. A previous study using ODI and

663 patch-wise circular variance measured using histology (measures variability in neurite

664 orientations) has shown that both measures have lower dispersion in demyelinated lesions in

665 patients with multiple sclerosis, where there is reduced geometrical complexity of neurites

666 (Grussu et al., 2017). The hippocampal gray matter has a general distribution of microstructure

667 that is similar to the neocortex, with tangential (proximal-distal) and radial (inner-outer)

668 components that follow the curvature of the hippocampus. In the current study we showed that

669 CA1 had the largest ODI, suggesting that it had the largest heterogeneity in neurite orientations.

670 CA1 has large tangential neural processes, like the Schaffer collaterals and perforant path, as

671 well as a large (yet dispersed) radial pyramidal cell layer (Duvernoy et al., 2013). By measuring

672 the orientation of the main direction of diffusion relative to the three hippocampal axes in CA1

673 (Figure 4), we found either high tangential or radial diffusion, supporting the idea that ODI

674 reflected the heterogeneity of these components. Conversely, ODI was lower in DG/CA4, CA3,

675 and at the most proximal edge of the subiculum. In these regions the primary diffusion direction

676 was minimally tangential or radial, and was mainly anterior-posterior or oblique with large

677 macroscopic diffusion anisotropy (i.e. large NDI and FA). The apparent reduction in

678 orientational heterogeneity (less radial/tangential components) and a resulting increase in

679 anisotropy may potentially explain the low ODI in these regions. In the DG/CA4 and CA3

680 region this could be a result of partial voluming with the nearby fimbria, and in the subiculum it

681 could be due to partial voluming with the nearby cingulum bundle or the perforant path at its

682 most proximal edge (supplementary Figure 11). As hypothesized in the rest of the cortex

683 (Fukutomi et al., 2018), it is likely that ODI in the hippocampal gray matter is largely driven by

684 the heterogeneity of radial and tangential neurite components.

685 *4.2 Hippocampal neurite density is highly correlated with T1w/T2w*

686 The distribution of the NDI and T1w/T2w across hippocampal gray matter was similar, as seen

687 in Figure 2D and E and as shown by their strong positive correlation and significant overlap.

688 While the diffusion signal is generally agnostic to water within myelin, previous work has shown

689 that myelinated axons restrict diffusion to a greater degree than unmyelinated axons (Behrens &

690 Johansen-Berg, 2014). This increase in restriction due to myelin would result in an increase in

691 NDI since there is more "stick" like diffusion occurring (i.e., a monoexponentially decaying

692 signal with a slope defined by the parallel diffusivity). Furthermore, due to the short exchange

693 time of water within dendrites and glia to the extra-cellular space, it is likely that any restricted

694 diffusion would be reflective of myelinated axons (Jespersen et al., 2010). This suggests that

695 NDI reflected the myelin content of the hippocampus. The T1w/T2w content and NDI were

696 largest in the body and tail of the subiculum. High myelin content in the subiculum has been

697   noted previously with histology (Ding & Van Hoesen, 2015). Furthermore, it is likely that the

698   white matter of the cingulum bundle or perforant path contribute to the large T1w/T2w content

699   seen in the subiculum. Conversely, T1w/T2w and NDI were lower in CA1, which is likely a

700   result of a relatively sparse layer of pyramidal cells along the midthickness surface or the largely

701   unmyelinated Schaffer collaterals (Jürgen et al., 2011; Szirmai et al., 2012). Overall, the

702   distribution of T1w/T2w found here agreed with previous studies (DeKraker et al., 2018;

703   Ábrahám et al., 2012). A strong positive correlation between NDI and T1w/T2w was found

704   previously across the cortex. However, the hippocampus was found to have high values in NDI

705   but low values of T1w/T2w when compared to the rest of the cortical areas (Fukutomi et al.,

706   2018). Here we showed that a strong correlation between NDI and T1w/T2w still exists in the

707   hippocampus when comparing them at a finer spatial scale. This correlation is further

708   corroborated by another cortical study at high ex vivo resolutions in the rodent brain, in which

709   cortical NDI was strongly correlated with staining intensity of myelinated axons (Jespersen et al.,

710   2010). Histological work has found similar correlations in white matter, where myelin content

711   was found to be strongly correlated with axon count (Schmierer et al., 2007). However, a recent

712   study utilizing a multicomponent relaxometry method for imaging myelin water fraction found

713   no significant correlation between myelin and NDI measured using NODDI in most white matter

714   structures (Qian et al., 2020). While NDI and T1w/T2w as a proxy of myelin do appear to be

715   correlated in gray matter including the hippocampus, further work is needed to examine this

716   correlation in other white matter structures, including white matter surrounding the hippocampus

717   such as the fimbria, fornix, and alveus.

718   *4.3 Microstructure metrics systematically vary across the subfields*

719   Microstructural metrics such as intra-cortical myelin and macrostructural cortical thickness have

720   been shown to be useful in parcellating the neocortex into subregions (Nieuwenhuys, 2013;

721   Glasser et al., 2014; Glasser & Van Essen, 2011). Furthermore, using non-negative matrix

722   factorization of T1w/T2w, MD, and FA it was found that a 4-component solution qualitatively

723   resembled hippocampal subfield borders (Patel et al., 2020), suggesting that T1w/T2w and

724   microstructure may provide sufficient separability to parcellate hippocampal subfields. In the

725   current study, by examining their averaged maps, we found that T1w/T2w, NDI, and ODI

726   appeared to be separable qualitatively across the subfields (Figure 2). Quantitatively, we showed

727   that a simple logistic regression model performed well in predicting the subfield label based on

728   the subfield-averaged metrics of T1w/T2w, NDI, and ODI. This result suggests that these

729   microstructural measures are potentially sensitive to the known microstructural differences

730   across the subfields as defined via cytoarchitectonics. Critically, it appeared that NDI and ODI

731   provided more separability across the subfields then FA and MD, suggesting that NODDI may

732   be more useful than DTI in capturing known microstructural differences across subfields

733   (supplementary Figure 6). CA2 appeared to be the exception, with a distinct pattern of MD when

734   compared to the other subfields, while this separability of CA2 was not captured with NODDI

735   metrics (supplementary Figure 6). Myelin content has been demonstrated previously to closely

736   correspond to averaged subfield borders (DeKraker et al., 2018). To a lesser extent,

737   macrostructure appeared to also follow the subfield borders, which has been noted previously for

738   thickness (DeKraker et al., 2018). While thickness is consistently low in CA3 and CA2, and

739   gyrification is consistently high in CA1, these measures alone may not differentiate all subfield

740   boundaries. Thus, a combination of NODDI and macrostructural measures may provide

741   complimentary information needed for subject-specific subfield delineation.

742   *4.4 The orientation of diffusion relative to the hippocampus may be useful in identifying*

743   *hippocampal microstructure*

744   We quantified the main direction of diffusion relative to the 3 main hippocampal axes which

745   microstructure tends to align closely with. Here we provide descriptions of microstructure

746   (Figure 1B) that likely contribute to the orientation results. The following three paragraphs

747   describe the anterior-posterior (AP), proximal-distal (PD), and inner-outer (IO) alignment,

748   respectively.

749   The high AP alignment in the body of the DG to CA3 was likely driven by the

750   neighbouring fimbria, the largest bundle in that region oriented AP. High AP alignment in the

751   subiculum was likely caused by the cingulum, a large fiber bundle that traverses the

752   parahippocampal gyrus. Some partial voluming from the outer (where the cingulum exists) to the

753   midthickness surface was expected, which may drive this alignment.

754   High PD alignment in the head of CA3 was expected to be either Schaffer collaterals

755   which curve immediately PD off of the apical dendrites of the pyramidal cells or from perforant

756   projections coming from the entorhinal cortex and entering CA3 which are also oriented PD.

757   High PD alignment in CA1 was likely a result of the Schaffer collaterals. The Schaffer

758   collaterals make synaptic contact at the apical and basal dendrites of CA1 in a PD fashion

759   (Nieuwenhuys et al., 2008; Swanson et al., 1978). However, the perforant path could have also

760   contributed to a higher PD alignment as it moves from the entorhinal cortex to the DG synapsing

761   on CA1 along the way (Nieuwenhuys et al., 2008). Furthermore, a high PD cosine similarity in

762   the CA3 region could have been a result of partial voluming with the alveus, a highly PD

763   oriented bundle that sits atop the hippocampal gray matter.

764   High IO alignment seen in CA1 was likely a result of the pyramidal neurons. The

765   pyramidal somas exist in the stratum pyramidale layer of the midthickness surface, and are

766   generally scattered in CA1 (Nieuwenhuys et al., 2008). Their axons and basal dendrites move IO

767   towards the alveus/outer surface and their large apical dendrites move IO towards the stratum

768   radiatum/inner surface. All IO alignment seen in CA1 was expected to be caused by the

769   pyramidal neurons or other afferent CA1 paths such as the Schaffer collaterals which may curve

770   IO before making contact with the apical dendrites of the pyramidal neurons. High IO alignment

771   in the subiculum was also likely caused by pyramidal neurons as in CA1.

772   The cosine similarities across subjects varied the greatest in CA1 and the subiculum across AP,

773   PD, and IO directions (supplementary Figure 7).

774   Typical hippocampal microstructural analyses average scalar diffusion metrics (such as

775   FA, MD, NDI, etc.) either across whole hippocampi (van Uden et al., 2015; Salmenpera et al.,

776   2006) or whole subfields (Radhakrishnan et al., 2020), which are inherently non-specific towards

777   microstructure that exists within and across subfields and the hippocampal long-axis. However,

778   tractography analyses which aim to capture the continuous intra-hippocampal circuitry are

779   difficult to perform, as at lower resolutions, tracts can be spurious requiring complex acquisition

780   and correction schemes (Zeineh et al., 2012). The orientational analyses described here have the

781   potential to increase specificity at in vivo resolutions by leveraging the known anatomical

782   orientations of hippocampal microstructure. Furthermore, capturing the essence of hippocampal

783   microstructural orientations with vertex-wise scalar values can make qualitative observations and

784   statistical analyses more tenable than with the complex 3D orientations provided by

785   tractography. Future studies could relate the hippocampal axis vectors to other dedicated

786   methods of diffusion orientation representation that have the ability to faithfully represent more

787   complex fiber configurations.

788   Applications of the proposed orientational methods may be useful to identify

789   microstructure deterioration in disease states, where affected microstructure may be less

790   prominent, and may appear as smaller cosine similarities along a particular axis. For example,

791   perforant path lesions in rats caused rapid memory loss which was akin to early-stage

792   Alzheimer's disease (Kirkby & Higgins, 2001). A 2010 study found deterioration of the

793   perforant path in aged humans using diffusion tensor imaging (Yassa et al., 2010). Perforant path

794   degradation should result in less attenuation of the diffusion signal along its length, which may

795   potentially show up as smaller PD cosine similarities specifically in the subiculum, CA3, and

796   CA1, as there should be less PD oriented diffusion. This may be possible for other neurological

797   diseases where specific microstructure is affected, such as pyramidal neuron degradation which

798   should result in smaller IO cosine similarities. However, to draw such conclusions, further ex

799   vivo validation with the ability to measure more ground-truth microstructural orientations will be

800   essential to evaluate the usefulness of this method. As well, future studies will have to evaluate

801   the efficacy of this method at clinical resolutions.

802   *4.5 6-component OPNNMF solution displays distinct co-varying regions of macro- and*

803   *microstructure*

804   The hippocampus is believed to have two main interacting dimensions of organization along its

805   medial-lateral/proximal-distal or subfield axis, and across its long or anterior-posterior axis (see

806   Genon et al., 2021 for review). In the current study with a 6-component OPNNMF solution we

807   found a gradient in the clusters along the proximal-distal direction, suggesting that regions along

808   this axis had disparate macro- and microstructural properties. That is, the macro- and

809   microstructural "axes" of the hippocampus as defined by the metrics used here tended to vary

810   along the same axis that the subfields were defined. Variability along this axis was expected, as

811   the subfields show differences in morphology, cytoarchitectonic profiles (Duvernoy et al., 2013;

812   Ding & Van Hoesen, 2015), and connectivity (Andersen et al., 1971), which likely manifest as

813   changes in macro- and microstructure. However, it is notable that a wide array of disparate

814   metrics at in vivo resolutions show such patterns. Recently there has been interest in the long-

815   axis organization of the hippocampus, with evidence coming from anatomical and physiological

816   recordings in rodents (Chase et al., 2015). In the current study there appeared to be a smaller

817   gradient in the clusters along the anterior-posterior axis, suggesting that the metrics used here

818   varied less along the long-axis when compared to the proximal-distal axis. While functional

819   studies have found stark variability across the long axis, it is unclear to the extent which the

820   hippocampal microstructure varies across this axis (Genon et al., 2021, Plachti et al., 2019).

821   Future work could look to examine the variability of dMRI measures across the long axis at

822   higher resolutions.

823   *4.6 Limitations*

824   There are some limitations of the current research that largely pertain to the metrics used here.

825   As noted in the introduction, DTI aims to capture the macroscopic diffusion anisotropy at each

826   voxel, assuming that the diffusion process can be well characterized by a Gaussian distribution.

827   Due to its popularity in both clinical and research settings, we sought to examine the distribution

828   of two common DTI measures (FA and MD) in the hippocampus. However, in most gray matter

829   regions there tends to be a complex arrangement of fiber orientations that cannot be well

830   modelled via a single tensor. This can result in drastically understated FA values with generally

831   spherical or planar DTI ellipsoids which contain minimal information on diffusion orientations

832   (Campbell et al., 2005). While DTI has been used extensively in the hippocampus, it has

833   generally been purported to be sensitive but not specific to its microstructure (Coras et al., 2014).

834   In ex vivo tissue at microscopic resolutions DTI metrics of FA and MD have shown good

835   contrast to the hippocampal laminae, demonstrating their sensitivity (Coras et al., 2014;

836   Shepherd et al., 2007; Stolp et al., 2018). However, at lower in vivo resolutions used here a

837   plethora of microstructure partial voluming within each voxel is inevitable, which leads to a

838   diffusion signal that may show little macroscopic diffusion anisotropy and thus cannot be

839   captured by a single tensor. Indeed, here we found that even the largest FA values of the

840   hippocampus in regions of purportedly high T1w/T2w tended to range around 0.28, a relatively

841   low amount of macroscopic anisotropy. Furthermore, it is unclear the extent to which extra-

842   hippocampal white matter such as the fimbria and angular bundle might influence our measures

843   sampled along the middle of the hippocampal gray matter.

844   The NODDI model has also been used extensively in both healthy and diseased states to

845   provide metrics that are biologically grounded. Such work involved explicitly modelling the

846 diffusion signal as a sum of compartments representing varying tissue geometries (Zhang et al.,

847 2012). However, some assumptions of the NODDI model are likely not valid in practice. The

848 tortuosity assumption that links the extra-cellular perpendicular diffusivity to the axon volume

849 fraction does not hold for tight axon packings (Jelescu et al., 2016). The NODDI model also sets

850 the intra-axonal parallel diffusivity equal to the extra-axonal parallel diffusivity. However, the

851 intra-axonal parallel diffusivity has been shown to be much higher than the extra-axonal parallel

852 diffusivity (Jelescu et al., 2016; Novikov et al., 2018). While we altered the fixed NODDI

853 diffusivity values to reflect what has been found in gray matter, the modelling degeneracies

854 mentioned here could influence the NODDI metrics, such that they may not correspond to the

855 biophysical reality of the tissue. To this end, there has been recent work which has sought to re-

856 structure the basic microstructural building blocks used for white matter modelling to improve

857 characterization of the gray matter. Two primary examples of this include a model which

858 accounts specifically for the presence of the soma (Palombo et al., 2020) and a model which

859 considers the water exchange across the cell membranes (i.e., from neurites to extra-cellular

860 space) (Jelescu et al., 2022). Future work should look to apply gray matter specific models in the

861 hippocampus.

862   Finally, the T1w/T2w ratio as a proxy for myelin content was used in the current study

863 based on previous work that demonstrated good correspondence with cortical patterns of myelin

864 distribution (Glasser & Van Essen 2011). However, recently it has been suggested that the

865 T1w/T2w ratio is a suboptimal proxy of myelin in the subcortex (Arshad et al., 2017). At

866 present, it is unclear whether the T1w/T2w ratio is also a suboptimal marker of myelin for

867 archicortical areas such as the hippocampus. Future work should look to investigate the use of

868 other techniques derived from quantitative MRI including magnetization transfer and myelin

869 water imaging to get an improved measure of myelin content within the hippocampus (Tardif et

870 al., 2016).

871 **5. Conclusion**

872 In the current study we show distinct in vivo microstructural distributions and orientations within

873 and across the hippocampal subfields, something that has not been investigated with comparable

874 granularity up to this point. Furthermore, we provide context for the use of surface-based

875 approaches to investigate hippocampal microstructure.

876 Our findings have several important implications for future work. The hippocampus is

877 particularly vulnerable to certain neurological diseases such as Alzheimer 's disease and

878 epilepsy, in which it is often one of the earliest aberrant structures (Dhikav et al., 2012).

879 Examining the microstructure of the hippocampus at fine spatial resolutions in the simplified

880 unfolded space, as done in this study, may provide potentially useful markers of hippocampal

881 integrity. Furthermore, we noticed relatively large radial and tangential components of diffusion

882 mainly in CA1 and the subiculum. Future work could attempt to tease apart these two

883 orientationally distinct populations, providing estimates which may be useful to examine

884 microstructurally specific deterioration. Furthermore, using the same orientation methods in this

885 study, future work should focus on capturing multiple microstructure orientations as the

886 hippocampus contains a complex configuration of fiber orientations. Future work could also

887 relate all the identified OPNNMF components to demographic and cognitive variables to identify

888 if there is a relationship between variability in cognitive performance and variability in the

889 metrics used in this study. Finally, the microstructural metrics observed in this study appear to

890 show good separability across hippocampal subfields, suggesting they may be sensitive to the

891 underlying cyto- and myeloarchitectonic differences.

892 **Acknowledgements**

References

907

908 Ábrahám, H., Vincze, A., Veszprémi, B., Kravják, A., Gömöri, É., Kovács, G. G., & Seress, L.

909   (2012). Impaired myelination of the human hippocampal formation in down syndrome.

910   *International Journal of Developmental Neuroscience*, *30*(2), 147–158.

911   https://doi.org/10.1016/j.ijdevneu.2011.11.005

912 Alexander-Bloch, A. F., Shou, H., Liu, S., Satterthwaite, T. D., Glahn, D. C., Shinohara, R. T.,

913   Vandekar, S. N., & Raznahan, A. (2018). On testing for spatial correspondence between

914   maps of human brain structure and function. *NeuroImage*, *178*, 540–551.

915   https://doi.org/10.1016/j.neuroimage.2018.05.070

916 Amunts, K., Lepage, C., Borgeat, L., Mohlberg, H., Dickscheid, T., Rousseau, M.-E., Bludau, S.,

917   Bazin, P.-L., Lewis, L. B., Oros-Peusquens, A.-M., Shah, N. J., Lippert, T., Zilles, K., &

918   Evans, A. C. (2013). Bigbrain: An ultrahigh-resolution 3d human brain model. *Science*,

919   *340*(6139), 1472–1475. https://doi.org/10.1126/science.1235381

920 Andersen, P., Bliss, T. V. P., & Skrede, K. K. (1971). Lamellar organization of hippocampal

921   excitatory pathways. *Experimental Brain Research*, *13*(2).

922   https://doi.org/10.1007/bf00234087

923 Andersson, J. L. R., & Sotiropoulos, S. N. (2015). Non-parametric representation and prediction

924   of single- and multi-shell diffusion-weighted MRI data using Gaussian processes.

925   *NeuroImage*, *122*, 166–176. https://doi.org/10.1016/j.neuroimage.2015.07.067

926 Arshad, M., Stanley, J. A., & Raz, N. (2017). Test-retest reliability and concurrent validity of in

927   vivo myelin content indices: Myelin water fraction and calibrated t1w/t2W image ratio.

928   *Human Brain Mapping*, *38*(4), 1780–1790. https://doi.org/10.1002/hbm.23481

929 Assaf, Y., & Basser, P. J. (2005). Composite hindered and restricted model of diffusion

930   (charmed) MR imaging of the human brain. *NeuroImage*, *27*(1), 48–58.

931   10.1016/j.neuroimage.2005.03.042

932 Assaf, Y., Blumenfeld-Katzir, T., Yovel, Y., & Basser, P. J. (2008). Axcaliber: A method for

933   measuring Axon diameter distribution from diffusion MRI. *Magnetic Resonance in*

934   *Medicine*, *59*(6), 1347–1354. 10.1002/mrm.21577

935 Assaf, Y., & Cohen, Y. (2000). Assignment of the water slow-diffusing component in the central

936   nervous system using Q-Space Diffusion Mrs: Implications for Fiber Tract Imaging.

937   *Magnetic   Resonance   in   Medicine*,   *43*(2),   191–199.

938   https://doi.org/10.1002/(sici)1522-2594(200002)43:2<191::aid-mrm5>3.0.co;2-b

939 Basser, P. J., Mattiello, J., & LeBihan, D. (1994). Mr diffusion tensor spectroscopy and

940   imaging. *Biophysical Journal*, *66*(1), 259–267.

941   https://doi.org/10.1016/s0006-3495(94)80775-1

942 Beaujoin, J., Palomero-Gallagher, N., Boumezbeur, F., Axer, M., Bernard, J., Poupon, F., . .

943   . Poupon, C. (2018). Post-mortem inference of the human Hippocampal connectivity

944   and microstructure using ultra-high field diffusion MRI at 11.7 T. *Brain Structure*

945   *and Function, 223*(5), 2157-2179.

946 Behrens, T., & Johansen-Berg, H. (2014). *Diffusion Mri: From quantitative measurement to*

947   *in vivo neuroanatomy*. Elsevier.

948 Bendel, O., Bueters, T., Euler, M. V., Ögren, S. O., Sandin, J., & Euler, G. V. (2005).

949   Reappearance of Hippocampal CA1 Neurons after Ischemia is Associated with

950   Recovery of Learning and Memory. *Journal of Cerebral Blood Flow & Metabolism,*

951   *25*(12), 1586-1595. 10.1038/sj.jcbfm.9600153

952 Blümcke, I., Coras, R., Miyata, H., & Özkara, C. (2012). Defining clinico-neuropathological

953   subtypes of Mesial Temporal Lobe Epilepsy with   hippocampal sclerosis. *Brain*

954   *Pathology*, *22*(3), 402–411. https://doi.org/10.1111/j.1750-3639.2012.00583.x

955   Boutsidis, C., & Gallopoulos, E. (2008). SVD based initialization: A head start for nonnegative

956   matrix   factorization.   *Pattern   Recognition*,   *41*(4),   1350–1362.

957   https://doi.org/10.1016/j.patcog.2007.09.010

958   Burggren, A. C., Zeineh, M. M., Ekstrom, A. D., Braskie, M. N., Thompson, P. M., Small, G.

959   W., & Bookheimer, S. Y. (2008). Reduced cortical thickness in hippocampal subregions

960   among cognitively normal apolipoprotein e E4 carriers. *NeuroImage*, *41*(4), 1177–1183.

961   https://doi.org/10.1016/j.neuroimage.2008.03.039

962   Campbell, J. S. W., Siddiqi, K., Rymar, V. V., Sadikot, A. F., & Pike, G. B. (2005). Flow-based

963   fiber tracking with diffusion tensor and Q-ball data: Validation and comparison to

964   principal diffusion direction techniques. *NeuroImage*, *27*(4), 725–736.

965   https://doi.org/10.1016/j.neuroimage.2005.05.014

966   Chase, H. W., Clos, M., Dibble, S., Fox, P., Grace, A. A., Phillips, M. L., & Eickhoff, S. B.

967   (2015). Evidence for an anterior–posterior differentiation in the human hippocampal

968   formation revealed by meta-analytic parcellation of fmri coordinate maps: Focus on the

969   Subiculum. *NeuroImage*, *113*, 44–60. https://doi.org/10.1016/j.neuroimage.2015.02.069

970   Cheng, H., Zhu, H., Zheng, Q., Liu, J., & He, G. (2020). Functional parcellation of the

971   hippocampus by semi-supervised clustering of resting state fmri data. *Scientific Reports*,

972   *10*(1). https://doi.org/10.1038/s41598-020-73328-1

973   Cherubini, E., & Miles, R. (2015). The CA3 region of the hippocampus: How is it? What

974   is it for? How does it do it? *Frontiers in Cellular Neuroscience, 9*.

975   10.3389/fncel.2015.00019

976   Coras, R., Milesi, G., Zucca, I., Mastropietro, A., Scotti, A., Figini, M., Mühlebner, A.,

977   Hess, A., Graf, W., Tringali, G., Blümcke, I., Villani, F., Didato, G., Frassoni, C.,

978   Spreafico, R., & Garbelli, R. (2014). 7T MRI features in control Human hippocampus

979   and hippocampal sclerosis: An ex vivo study with histologic correlations. *Epilepsia*,

980   *55*(12), 2003–2016. https://doi.org/10.1111/epi.12828

981   DeKraker, J., Ferko, K., Lau, J., Köhler, S., & Khan, A. (2018). Unfolding the hippocampus: An

982   intrinsic coordinate system for subfield segmentations and quantitative mapping.

983   *NeuroImage, 167*, 408418. 10.1016/j.neuroimage.2017.11.054

984   DeKraker, J., Haast, R. A. M., Yousif, M. D., Karat, B., Lau, J. C., Köhler, S., & Khan, A. R.

985   (2022). Automated hippocampal unfolding for morphometry and subfield segmentation

986   with Hippunfold. *ELife*, *11*. https://doi.org/10.7554/elife.77945

987   DeKraker, J., Köhler, S., & Khan, A. R. (2021). Surface-based hippocampal subfield

988   segmentation. *Trends in Neurosciences*. https://doi.org/10.1016/j.tins.2021.06.005

989   DeKraker, J., Lau, J. C., Ferko, K. M., Khan, A. R., & Köhler, S. (2020). Hippocampal

990   subfields revealed through unfolding and unsupervised clustering of laminar and

991   morphological features in 3D BigBrain. *NeuroImage*, *206*, 116328.

992   https://doi.org/10.1016/j.neuroimage.2019.116328

993   Dhikav, V., & Anand, K. S. (2012). Hippocampus in health and disease: An overview. *Annals of*

994   *Indian Academy of Neurology*, *15*(4), 239. https://doi.org/10.4103/0972-2327.104323

995   Ding, S.-L., & Van Hoesen, G. W. (2015). Organization and detailed parcellation of human

996   hippocampal head and body regions based on a combined analysis of cyto- and

997   chemoarchitecture. *Journal of Comparative Neurology*, *523*(15), 2233–2253.

998   https://doi.org/10.1002/cne.23786

999   Dinkelacker, V., Valabregue, R., Thivard, L., Lehéricy, S., Baulac, M., Samson, S., &

1000   Dupont, S. (2015). Hippocampal-thalamic wiring in medial temporal lobe epilepsy:

1001   Enhanced connectivity per hippocampal voxel. *Epilepsia*, *56*(8), 1217–1226.

1002   https://doi.org/10.1111/epi.13051

1003 Duvernoy, H. M., Cattin, F., & Risold, P.-Y. (2013). *The human hippocampus functional*

1004   *anatomy, vascularization and serial sections with MRI*. Springer.

1005 Fukutomi, H., Glasser, M. F., Murata, K., Akasaka, T., Fujimoto, K., Yamamoto, T., Autio, J.

1006   A., Okada, T., Togashi, K., Zhang, H., Van Essen, D. C., & Hayashi, T. (2019).

1007   Diffusion tensor model links to neurite orientation dispersion and density imaging at

1008   high B-value in cerebral cortical gray matter. Scientific Reports, 9(1).

1009   https://doi.org/10.1038/s41598-019-48671-7

1010 Fukutomi, H., Glasser, M. F., Zhang, H., Autio, J. A., Coalson, T. S., Okada, T., Togashi,

1011   K., Van Essen, D. C., & Hayashi, T. (2018). Neurite imaging reveals

1012   microstructural variations in human cerebral cortical gray matter. *NeuroImage*, *182*,

1013   488–499.10.1016/j.neuroimage.2018.02.017

1014 Garcia, K. E., Kroenke, C. D., & Bayly, P. V. (2018). Mechanics of cortical folding: Stress,

1015   growth and stability. *Philosophical Transactions of the Royal Society B: Biological*

1016   *Sciences*, *373*(1759), 20170321. https://doi.org/10.1098/rstb.2017.0321

1017 Garyfallidis, E., Brett, M., Amirbekian, B., Rokem, A., van der Walt, S., Descoteaux, M., &

1018   Nimmo-Smith, I. (2014). Dipy, a library for the analysis of diffusion MRI data.

1019   *Frontiers in Neuroinformatics*, *8*. https://doi.org/10.3389/fninf.2014.00008

1020 Genon, S., Bernhardt, B. C., La Joie, R., Amunts, K., & Eickhoff, S. B. (2021). The many

1021   dimensions of human hippocampal organization and (dys)function. *Trends in*

1022   *Neurosciences*, *44*(12), 977–989. https://doi.org/10.1016/j.tins.2021.10.003

1023 Glasser, M. F., & Van Essen, D. C. (2011). Mapping human cortical areas in vivo based on

1024   myelin content as revealed by T1- and T2-weighted MRI. *Journal of Neuroscience*,

1025   *31*(32), 11597–11616. https://doi.org/10.1523/jneurosci.2180-11.2011

1026   Glasser, M. F., Sotiropoulos, S. N., Wilson, J. A., Coalson, T. S., Fischl, B., Andersson, J. L.,

1027   Xu, J., Jbabdi, S., Webster, M., Polimeni, J. R., Van Essen, D. C., & Jenkinson, M.

1028   (2013).

1029   The minimal preprocessing pipelines for the Human Connectome Project. *NeuroImage*,

1030   *80*, 105–124. https://doi.org/10.1016/j.neuroimage.2013.04.127

1031   Glasser, M. F., Goyal, M. S., Preuss, T. M., Raichle, M. E., & Van Essen, D. C. (2014). Trends

1032   and properties of human cerebral cortex: Correlations with cortical myelin content.

1033   *NeuroImage*, *93*, 165–175. https://doi.org/10.1016/j.neuroimage.2013.03.060

1034   Goodroe, S. C., Starnes, J., & Brown, T. I. (2018). The Complex Nature of

1035   Hippocampal-Striatal Interactions in Spatial Navigation. *Frontiers in Human*

1036   *Neuroscience, 12*. 10.3389/fnhum.2018.00250

1037   Grussu, F., Schneider, T., Tur, C., Yates, R. L., Tachrount, M., Ianuş, A., Yiannakas, M. C.,

1038   Newcombe, J., Zhang, H., Alexander, D. C., DeLuca, G. C., & Gandini Wheeler-

1039   Kingshott, C. A. (2017). ? *Annals of Clinical and Translational Neurology*, *4*(9), 663–

1040   679. https://doi.org/10.1002/acn3.445

1041   Guerrero, J. M., Adluru, N., Bendlin, B. B., Goldsmith, H. H., Schaefer, S. M., Davidson, R. J.,

1042   Kecskemeti, S. R., Zhang, H., & Alexander, A. L. (2019). Optimizing the fitting initial

1043   condition for the parallel intrinsic diffusivity in NODDI: An extensive empirical

1044   evaluation. https://doi.org/10.1101/630541

1045   Halko, N., Martinsson, P. G., & Tropp, J. A. (2011). Finding structure with randomness:

1046   Probabilistic algorithms for constructing approximate matrix decompositions. *SIAM*

1047   *Review*, *53*(2), 217–288. https://doi.org/10.1137/090771806

1048   Harms, R. L., Fritz, F. J., Tobisch, A., Goebel, R., & Roebroeck, A. (2017). Robust and fast

1049   nonlinear optimization of diffusion mri microstructure models. *NeuroImage*, *155*, 82–96.

1050   https://doi.org/10.1016/j.neuroimage.2017.04.064

1051   Horner, A. J., Bisby, J. A., Bush, D., Lin, W., & Burgess, N. (2015). Evidence for holistic

1052   episodic recollection via hippocampal pattern completion. *Nature Communications, 6*(1).

1053   10.1038/ncomms8462

1054   Isensee, F., Jaeger, P. F., Kohl, S. A., Petersen, J., & Maier-Hein, K. H. (2020). NNU-net: A

1055   self-configuring method for deep learning-based biomedical image segmentation. *Nature*

1056   *Methods*, *18*(2), 203–211. https://doi.org/10.1038/s41592-020-01008-z

1057   Jelescu, I. O., Veraart, J., Adisetiyo, V., Milla, S. S., Novikov, D. S., & Fieremans, E. (2015).

1058   One diffusion acquisition and different white matter models: How does microstructure

1059   change in human early development based on WMTI and Noddi? *NeuroImage*, *107*,

1060   242–256. https://doi.org/10.1016/j.neuroimage.2014.12.009

1061   Jelescu, I. O., Veraart, J., Fieremans, E., & Novikov, D. S. (2016). Degeneracy in model

1062   parameter estimation for multi-compartmental diffusion in neuronal tissue. *NMR in*

1063   *Biomedicine*, *29*(1), 33–47. https://doi.org/10.1002/nbm.3450

1064   Jelescu, I. O., de Skowronski, A., Geffroy, F., Palombo, M., & Novikov, D. S. (2022). Neurite

1065   Exchange Imaging (NEXI): A minimal model of diffusion in gray matter with inter-

1066   compartment water exchange. *NeuroImage*, *256*, 119277.

1067   https://doi.org/10.1016/j.neuroimage.2022.119277

1068   Jenkinson, M., Bannister, P., Brady, M., & Smith, S. (2002). Improved optimization for the

1069   robust and accurate linear registration and motion correction of brain images.

1070   *NeuroImage*, *17*(2), 825–841. https://doi.org/10.1006/nimg.2002.1132

1071   Jespersen, S. N., Bjarkam, C. R., Nyengaard, J. R., Chakravarty, M. M., Hansen, B., Vosegaard,

1072   T., Østergaard, L., Yablonskiy, D., Nielsen, N. C., & Vestergaard-Poulsen, P. (2010).

1073   Neurite density from magnetic resonance diffusion measurements at ultrahigh field:

1074   Comparison with light microscopy and electron microscopy. *NeuroImage*, *49*(1),

1075   205–216. https://doi.org/10.1016/j.neuroimage.2009.08.053

1076   Jürgen M. K., Paxinos, G., Insausti, R., & Amaral, D. G. (2011). Hippocampal Formation. In *The*

1077   *Human Nervous System* (3rd ed., pp. 871–914). Elsevier Academic Press.

1078   Karat., B (2023). Bradley-Karat/Hippo_Spin_Testing; 0.1.0 (v0.1.0). Zenodo.

1079   https://doi.org/10.5281/zenodo.7837990

1080   Kirkby, D. L., & Higgins, G. A. (2001). Characterization of perforant path lesions in rodent

1081   models of memory and attention. *European Journal of Neuroscience*, *10*(3), 823–838.

1082   https://doi.org/10.1046/j.1460-9568.1998.00087.x

1083   Knierim, J. J. (2015). The hippocampus. *Current Biology, 25*(3), R1116-R1121.

1084   La Joie, R., Perrotin, A., de La Sayette, V., Egret, S., Doeuvre, L., Belliard, S., Eustache, F.,

1085   Desgranges, B., & Chételat, G. (2013). Hippocampal subfield volumetry in mild

1086   cognitive impairment, Alzheimer's disease and semantic dementia. *NeuroImage:*

1087   *Clinical*,

1088   *3*, 155–162. https://doi.org/10.1016/j.nicl.2013.08.007

1089   Liu, C., Ye, F. Q., Newman, J. D., Szczupak, D., Tian, X., Yen, C. C.-C., Majka, P., Glen, D.,

1090   Rosa, M. G., Leopold, D. A., & Silva, A. C. (2020). A resource for the detailed 3D

1091   mapping of white matter pathways in the marmoset brain. *Nature Neuroscience*, *23*(2),

1092   271–280. https://doi.org/10.1038/s41593-019-0575-0

1093   Maillot, J., Yahia, H., & Verroust, A. (1993). Interactive texture mapping. *Proceedings of the*

1094   *20th Annual Conference on Computer Graphics and Interactive Techniques -*

1095   *SIGGRAPH '93*. https://doi.org/10.1145/166117.166120

1096   Moodley, K. K., & Chan, D. (2014). The hippocampus in neurodegenerative disease. *Frontiers*

1097   *of Neurology and Neuroscience*, 95–108. https://doi.org/10.1159/000356430

1098 Nieuwenhuys, R., Huijzen, C. van, & Voogd, J. (2008). *The human central nervous system*.

1099   Springer.

1100 Nieuwenhuys, R. (2013). The myeloarchitectonic studies on the human cerebral cortex of the

1101   Vogt-vogt school, and their significance for the interpretation of functional neuroimaging

1102   data. *Microstructural Parcellation of the Human Cerebral Cortex*, 55–125.

1103   https://doi.org/10.1007/978-3-662-45766-5_3

1104 Novikov, D. S., Veraart, J., Jelescu, I. O., & Fieremans, E. (2018). Rotationally-invariant

1105   mapping of scalar and orientational metrics of neuronal microstructure with diffusion

1106   MRI. *NeuroImage*, *174*, 518–538. https://doi.org/10.1016/j.neuroimage.2018.03.006

1107 Ozarslan, E., Koay, C.G., Shepherd, T., Blackband, S., & Basser, P. (2009). Simple harmonic

1108   oscillator based reconstruction and estimation for three-dimensional q-space MRI.

1109   *Proceedings of the International Society for Magnetic Resonance in Medicine,* 16.

1110 Palombo, M., Ianus, A., Guerreri, M., Nunes, D., Alexander, D. C., Shemesh, N., & Zhang, H.

1111   (2020). SANDI: A compartment-based model for non-invasive apparent Soma and neurite

1112   imaging by Diffusion MRI. *NeuroImage*, *215*, 116835.

1113   https://doi.org/10.1016/j.neuroimage.2020.116835

1114 Patel, R., Steele, C. J., Chen, A. G. X., Patel, S., Devenyi, G. A., Germann, J., Tardif, C. L., &

1115   Chakravarty, M. M. (2020). Investigating microstructural variation in the human

1116   hippocampus using non-negative matrix factorization. *NeuroImage*, *207*, 116348.

1117   https://doi.org/10.1016/j.neuroimage.2019.116348

1118 Pedregosa, F., Varoquaux, G., Gramfort, A., Michel, V., Thirion, B., Grisel, O., Blondel, M.,

1119   Prettenhofer, P., Weiss, R., Dubourg, V., Vanderplas, J., Passos, A., Cournapeau, D.,

1120   Brucher, M., Perrot, M., & Duchesnay, É. (2011). Scikit-learn: Machine Learning in

1121   Python. *Journal of Machine Learning Research*, *12*(85), 2825–2830.

1122   Pierpaoli, C., Jezzard, P., Basser, P. J., Barnett, A., & Di Chiro, G. (1996). Diffusion tensor MR

1123   imaging of the human brain. *Radiology*, *201*(3), 637–648.

1124   https://doi.org/10.1148/radiology.201.3.8939209

1125   Plachti, A., Eickhoff, S. B., Hoffstaedter, F., Patil, K. R., Laird, A. R., Fox, P. T., Amunts, K., &

1126   Genon, S. (2019). Multimodal parcellations and extensive behavioral profiling tackling

1127   the hippocampus gradient. *Cerebral Cortex*, *29*(11), 4595–4612.

1128   https://doi.org/10.1093/cercor/bhy336

1129   Plachti, A., Kharabian, S., Eickhoff, S. B., Maleki Balajoo, S., Hoffstaedter, F., Varikuti, D. P.,

1130   Jockwitz, C., Caspers, S., Amunts, K., & Genon, S. (2020). Hippocampus co-atrophy

1131   pattern in dementia deviates from covariance patterns across the lifespan. *Brain*, *143*(9),

1132   2788–2802. https://doi.org/10.1093/brain/awaa222

1133   Poppenk, J., Evensmoen, H. R., Moscovitch, M., & Nadel, L. (2013). Long-axis specialization

1134   of the human hippocampus. *Trends in Cognitive Sciences*, *17*(5), 230–240.

1135   https://doi.org/10.1016/j.tics.2013.03.005

1136   Qian, W., Khattar, N., Cortina, L. E., Spencer, R. G., & Bouhrara, M. (2020). Nonlinear

1137   associations of neurite density and myelin content with age revealed using

1138   multicomponent diffusion and relaxometry magnetic resonance imaging. *NeuroImage*,

1139   *223*, 117369. https://doi.org/10.1016/j.neuroimage.2020.117369

1140   Quezada, S., van de Looij, Y., Hale, N., Rana, S., Sizonenko, S. V., Gilchrist, C.,

1141   Castillo-Melendez, M., Tolcos, M., & Walker, D. W. (2020). Genetic and

1142   microstructural differences in the cortical plate of gyri and sulci during gyrification in

1143   fetal sheep. *Cerebral Cortex*, *30*(12), 6169–6190. https://doi.org/10.1093/cercor/bhaa171

1144   Radhakrishnan, H., Stark, S. M., & Stark, C. E. (2020). Microstructural alterations in

1145   Hippocampal Subfields Mediate Age-related Memory decline in humans. *Frontiers in*

1146   *Aging Neuroscience*, *12*. https://doi.org/10.3389/fnagi.2020.00094

1147 Raffelt, D. A., Tournier, J.-D., Smith, R. E., Vaughan, D. N., Jackson, G., Ridgway, G. R., &

1148 Connelly, A. (2017). Investigating white matter fibre density and morphology using

1149 fixel-based analysis. *NeuroImage*, *144*, 58–73.

1150 https://doi.org/10.1016/j.neuroimage.2016.09.029

1151 Robinson, J. L., Barron, D. S., Kirby, L. A., Bottenhorn, K. L., Hill, A. C., Murphy, J. E., Katz,

1152 J.S., Salibi, N., Eickhoff, S. B., & Fox, P. T. (2015). Neurofunctional topography of the

1153 human hippocampus. *Human Brain Mapping*, *36*(12), 5018–5037.

1154 https://doi.org/10.1002/hbm.22987

1155 Salmenpera, T. M., Simister, R. J., Bartlett, P., Symms, M. R., Boulby, P. A., Free, S. L.,

1156 Barker, G. J., & Duncan, J. S. (2006). High-resolution diffusion tensor imaging of the

1157 hippocampus in temporal lobe epilepsy. *Epilepsy Research*, *71*(2-3), 102–106.

1158 https://doi.org/10.1016/j.eplepsyres.2006.05.020

1159 Schmierer, K., Wheeler-Kingshott, C. A. M., Boulby, P. A., Scaravilli, F., Altmann, D. R.,

1160 Barker, G. J., Tofts, P. S., & Miller, D. H. (2007). Diffusion tensor imaging of Post

1161 Mortem Multiple Sclerosis Brain. *NeuroImage*, *35*(2), 467–477.

1162 https://doi.org/10.1016/j.neuroimage.2006.12.010

1163 Shepherd, T. M., Özarslan, E., Yachnis, A. T., King, M. A., & Blackband, S. J. (2007).

1164 Diffusion Tensor Microscopy Indicates the Cytoarchitectural Basis for Diffusion

1165 Anisotropy in the Human Hippocampus. *American Journal of Neuroradiology*, *28*(5),

1166 958–964.

1167 Small, S. A., Schobel, S. A., Buxton, R. B., Witter, M. P., & Barnes, C. A. (2011). A

1168 pathophysiological framework of hippocampal dysfunction in ageing and disease. *Nature*

1169 *Reviews Neuroscience*, *12*(10), 585–601. https://doi.org/10.1038/nrn3085

1170 Sotiras, A., Resnick, S. M., & Davatzikos, C. (2015). Finding imaging patterns of structural

1171 covariance via non-negative matrix factorization. *NeuroImage*, *108*, 1–16.

1172   https://doi.org/10.1016/j.neuroimage.2014.11.045

1173   Sotiropoulos, S. N., Moeller, S., Jbabdi, S., Xu, J., Andersson, J. L., Auerbach, E. J., Yacoub,

1174   E., Feinberg, D., Setsompop, K., Wald, L. L., Behrens, T. E., Ugurbil, K., & Lenglet, C.

1175   (2013). Effects of image reconstruction on fiber orientation mapping from multichannel

1176   diffusion mri: Reducing the noise floor using sense. *Magnetic Resonance in Medicine*,

1177   *70*(6), 1682–1689. https://doi.org/10.1002/mrm.24623

1178   Stolp, H. B., Ball, G., So, P.-W., Tournier, J.-D., Jones, M., Thornton, C., & Edwards, A. D.]

1179   (2018). Voxel-wise comparisons of cellular microstructure and diffusion-MRI in mouse

1180   hippocampus using 3D bridging of optically-clear histology with neuroimaging data (3D-

1181   bond). *Scientific Reports*, *8*(1). https://doi.org/10.1038/s41598-018-22295-9

1182   Strang, B. A., Witter, M. P., Lein, E. S., & Moser, E. I. (2014). Functional organization of the

1183   Hippocampal Longitudinal Axis. *Nature Reviews Neuroscience*, *15*(10), 655–669.

1184   https://doi.org/10.1038/nrn3785

1185   Swanson, L. W., Wyss, J. M., & Cowan, W. M. (1978). An autoradiographic study of the

1186   organization of intrahippocampal association pathways in the rat. *The Journal of

1187   Comparative Neurology*, *181*(4), 681–715. https://doi.org/10.1002/cne.901810402

1188   Szirmai, I., Buzsáki, G., & Kamondi, A. (2012). 120 years of hippocampal Schaffer Collaterals.

1189   *Hippocampus*, *22*(7), 1508–1516. https://doi.org/10.1002/hipo.22001

1190   Tardif, C. L., Gauthier, C. J., Steele, C. J., Bazin, P.-L., Schäfer, A., Schaefer, A., Turner, R., &

1191   Villringer, A. (2016). Advanced MRI techniques to improve our understanding of

1192   experience-induced neuroplasticity. *NeuroImage*, *131*, 55–72.

1193   https://doi.org/10.1016/j.neuroimage.2015.08.047

1194   Van Essen, D., Smith, S., Barch, D., Behrens, T., Yacoub, E., & Ugurbil, K. (2013). The

1195   WU-Minn Human Connectome Project: An overview. *NeuroImage, 80*(62), 62-79.

1196   van Uden, I. W. M., Tuladhar, A. M., van der Holst, H. M., van Leijsen, E. M. C., van

1197   Norden, A. G. W., de Laat, K. F., Rutten-Jacobs, L. C. A., Norris, D. G., Claassen, J. A.

1198   H. R., van Dijk, E. J., Kessels, R. P. C., & de Leeuw, F.-E. (2015). Diffusion tensor

1199   imaging of the HIPPOCAMPUS predicts the risk of dementia; the RUN DMC study.

1200   *Human Brain Mapping*, *37*(1), 327–337. https://doi.org/10.1002/hbm.23029

1201   Voss, J. L., Bridge, D. J., Cohen, N. J., & Walker, J. A. (2017). A Closer Look at the

1202   Hippocampus and Memory. *Trends in Cognitive Sciences, 21*(8), 577-588.

1203   10.1016/j.tics.2017.05.008

1204   Yang, & Oja, E. (2010). Linear and nonlinear projective nonnegative matrix factorization. *IEEE*

1205   *Transactions   on   Neural   Networks*,   *21*(5),   734–749.

1206   https://doi.org/10.1109/tnn.2010.2041361

1207   Yassa, M. A., Muftuler, L. T., & Stark, C. E. (2010). IC-P-056: Microstructural diffusion tensor

1208   Imaging reveals perforant path degradation in aged humans in vivo. *Alzheimer's &*

1209   *Dementia, 6*.

1210   Yushkevich, P. A., Wang, H., Pluta, J., Das, S. R., Craige, C., Avants, B. B., Weiner, M. W., &

1211   Mueller, S. (2011). Nearly automatic segmentation of hippocampal subfields in in vivo

1212   focal T2-weighted MRI. *NeuroImage*, *53*(4), 1208–1224.

1213   https://doi.org/10.1016/j.neuroimage.2010.06.040

1214   Zeineh, M. M., Holdsworth, S., Skare, S., Atlas, S. W., & Bammer, R. (2012). Ultra-high

1215   resolution diffusion tensor imaging of the microscopic pathways of the medial temporal

1216   lobe. *NeuroImage, 62*(3), 2065-2082.

1217   Zeineh, M. M., Palomero-Gallagher, N., Axer, M., Gräβel, D., Goubran, M., Wree, A., Woods,

1218   R., Amunts, K., & Zilles, K. (2017). Direct visualization and mapping of the spatial course

1219   of fiber tracts at microscopic resolution in the Human Hippocampus. *Cerebral Cortex*.

1220   https://doi.org/10.1093/cercor/bhw010

1221   Zhang, H., Schneider, T., Wheeler-Kingshott, C. A., & Alexander, D. C. (2012). NODDI:

1222   Practical in vivo neurite orientation dispersion and density imaging of the human brain.

1223   *NeuroImage, 61*(4), 1000-1016. 10.1016/j.neuroimage.2012.03.072

1224   Zhong, Q., Xu, H., Qin, J., Zeng, L.-L., Hu, D., & Shen, H. (2019). Functional parcellation of the

1225   hippocampus from resting-state dynamic functional connectivity. *Brain Research*, *1715*,

1226   165–175. https://doi.org/10.1016/j.brainres.2019.03.023

1227   Zhou, Y., Dougherty, J. H., Hubner, K. F., Bai, B., Cannon, R. L., & Hutson, R. K. (2008).

1228   Abnormal connectivity in the posterior cingulate and hippocampus in early alzheimer's

1229   disease and mild cognitive impairment. *Alzheimer's & Dementia*, *4*(4), 265–270.

1230   https://doi.org/10.1016/j.jalz.2008.04.006